Emitted Power Of Jupiter

Based On Cassini CIRS And VIMS Observations

Liming Li[1*], Kevin H. Baines[2], Mark A. Smith[1], Robert A. West[2], Santiago Perez-Hoyos[3], Harold J. Trammel[1], Amy A. Simon-Miller[4], Barney J. Conrath[5], Peter J. Gierasch[5], Glenn S. Orton[2], Conor A. Nixon[6], Gianrico Filacchione[7], Patrick M. Fry[8], Thomas W. Momary[2]

[1] *Department of Physics, University of Houston, Houston, TX 77204, USA.*

[2] *Jet Propulsion Laboratory, Caltech, Pasadena, CA, 91109, USA.*

[3] *Dpto, Fisica Aplicada I, E.T.S. Ingenieria UPV/EHU, c/Alda. Urquijo s/n, 48013 Bilbao, Spain.*

[4] *NASA Goddard Space Flight Center, Greenbelt, MD 20771, USA.*

[5] *Department of Astronomy, Cornell University, Ithaca, NY 14853, USA.*

[6] *Department of Astronomy, University of Maryland, College Park, MD 20742, USA.*

[7] *INAF-IAPS, Istituto di Astrofisica e Planetologia Spaziali, Area di Ricerca di Tor Vergata, via del Fosso del Cavaliere, 100, 00133, Rome, Italy.*

[8] *Space Science and Engineering Center, University of Wisconsin, Madison, WI 53706, USA.*

[*] To whom all correspondence should be addressed. E-mail: lli7@uh.mail.edu

ABSTRACT

The emitted power of Jupiter and its meridional distribution are determined from observations by the Composite Infrared Spectrometer (CIRS) and Visual and Infrared Spectrometer (VIMS) onboard Cassini during its flyby en route to Saturn in late 2000 and early 2001. Jupiter's global-average emitted power and effective temperature are measured to be 14.10±0.03 Wm^{-2} and 125.57±0.07 K, respectively. On a global scale, Jupiter's 5-μm thermal emission contributes ~ 0.7±0.1% to the total emitted power at the global scale, but it can reach ~ 1.9±0.6% at 15°N. The meridional distribution of emitted power shows a significant asymmetry between the two hemispheres with the emitted power in the northern hemisphere 3.0±0.3% larger than that in the southern hemisphere. Such an asymmetry shown in the Cassini epoch (2000-01) is not present during the Voyager epoch (1979). In addition, the global-average emitted power increased ~ 3.8±1.0% between the two epochs. The temporal variation of Jupiter's total emitted power is mainly due to the warming of atmospheric layers around the pressure level of 200 mbar. The temporal variation of emitted power was also discovered on Saturn (Li et al., 2010). Therefore, we suggest that the varying emitted power is a common phenomenon on the giant planets.

1) INTRODUCTION

The absorbed solar radiance and the emitted thermal emission determine the energy budget of an astronomical body. For three of the four giant planets in our solar system (i.e., Jupiter, Saturn, and Neptune), large energy imbalances between the absorbed solar radiance and the emitted thermal emission were discovered and hence the internal heat was inferred. Such large energy imbalances and internal heat have important implications for atmospheric circulation and planetary formation/evolution, as reviewed in two related studies (Conrath et al., 1989; Hanel et al., 2003) and in our previous study of Saturn's emitted power (Li et al., 2010).

Previous observations of Jupiter (Ingersoll et al., 1975; Hanel et al., 1981; Pirraglia, 1984) have provided some important characteristics of the energy budget, the internal heat, and their meridional distributions. However, the temporal variability of the energy budget for Jupiter has not been explored mainly due to the limited observation set. Yet, it provides valuable clues for examining the time scale of internal heat referred from the theories of planetary formation/evolution (Smoluchowski, 1967; Salpeter, 1973; Flasar, 1973; Stevenson and Salpeter, 1977; Grossman et al., 1980; Guillot et al., 2004). In addition, the meridional distribution of energy budget and its temporal variation provide insights into atmospheric dynamics and general circulation (Pirraglia, 1984; Friedson and Ingersoll, 1987). The measurements of Jupiter's energy budget set important constraints on the heating/cooling rates as a function of altitude in the jovian atmosphere, following a similar study for the saturnian atmosphere (Perez-Hoyos and Sanchez-Lavega, 2006). The exploration of the heating/cooling rates and their temporal variation will help us study the atmospheric circulation and dynamics on Jupiter. As well, the temporal variation of the energy budget also provides one more perspective on Jupiter's climatology. The

73 decadal-scale variation of cloud activity and the related convection has been characterized on
74 Jupiter (Baines et al., 2007). Moist convection is inferred to be a prime transporter of internal
75 heat on Jupiter (Gierasch et al., 2000; Ingersoll et al., 2000). Therefore, measurements of the
76 temporal variation of the internal heat help determine if the decadal variation of convection and
77 hence cloud variability acts as a valve that varies the flux from the interior of Jupiter and further
78 adjusts possible climate change (Marcus, 2000).
79
80 The Cassini observations provide an opportunity to revisit the energy budget on Jupiter.
81 Furthermore, the combination of the Cassini observations and the previous observations provides
82 an opportunity to explore its temporal variability. This study is the first of a series of studies
83 examining the temporal variability of the energy budget on Jupiter. In this study, we present the
84 exploration of Jupiter's emitted power as determined by Cassini observations, and compare it
85 with previous measurements from Pioneer/Voyager (Ingersoll et al., 1975; Hanel et al., 1981;
86 Pirraglia, 1984). Observations from Earth-based and airborne telescopes are not included in this
87 study because of the relatively large uncertainties and the discrepancies among them (please
88 refer to Table 1 in Hanel et al., 1981 and Table I in Conrath et al., 1989). Note: planetographic
89 latitude is used in this study. In addition, the solar longitude, which is defined as the angular
90 distance along Jupiter's orbit around Sun measured from a reference point in the orbit (i.e., the
91 zero of solar longitude at northern spring equinox), is used to track the different seasons.
92
93 **2) METHODOLOGY**
94 The methodology of computing a planet's emitted power (i.e., the emitted energy per unit time
95 over a unit area) with the Cassini observations was introduced in our previous study of Saturn's

96 emitted power (Li et al., 2010). The basic idea is that we will integrate recorded radiance over
97 emission angle and wavelength to obtain Jupiter's emitted power.
98
99 In comparison to the on-orbit long-term (2004-) observations of Saturn, the Jupiter flyby
100 observations by Cassini are somewhat limited in the coverage of emission angle. To fill the
101 observational gaps in the coverage of emission angle, additional techniques (e.g., linear
102 regression) are needed beyond the least-squares fit method (see Section 4). In addition, the
103 thermal emission near 5 μm is significantly strong on Jupiter (Westphal, 1969), and is thus
104 included in our computation of Jupiter's emitted power (Conrath et al., 1989).
105
106 Finally, the method of addressing the dependence of atmospheric radiance upon the emission
107 angle is different between this Cassini study and the previous Voyager studies (Pirraglia, 1984,
108 Ingersoll, 1990). In the Cassini analysis, the least-squares fit and the linear regression are used to
109 fill the observational gaps in the emission angle (please see Section 4). Such a method does not
110 require the knowledge of the temperature structure and chemical components of Jupiter's
111 atmosphere. The Voyager observations has much less coverage in the emission angle than the
112 coverage in the Cassini observations in the middle infrared (i.e., FP3 and FP4), so the method of
113 the least-square fit does not work for filling the observations gaps in the Voyager observations.
114 Instead, the dependence of the atmospheric radiance upon the emission angle was addressed by
115 the radiative-transfer calculations with the retrieved atmospheric temperature and opacity (Hanel
116 et al., 1981) in the previous Voyager studies (Pirraglia, 1984),(also see Section 4).
117
118 **3) CASSINI OBSERVATIONS AND DATA PROCESSING**

119 The measurements of Jupiter's emitted power are based on the Cassini observations obtained
120 during the period of the Jupiter flyby, from October 1, 2000 to March 22, 2001. We use the
121 observations from two instruments. The Composite Infrared Spectrometer (CIRS) measures the
122 great majority of the outgoing thermal emission of Jupiter with wavelengths from 7 to 1000 μm.
123 The Visual and Infrared Mapping Spectrometer (VIMS) records the 5-μm thermal emission. The
124 two instruments and the corresponding data processing are described below.
125
126 **3.1) Cassini/CIRS Observations**
127 The CIRS instrument (Flasar et al., 2004a) acquires Jupiter's spectra in three focal planes: FP1,
128 FP3, and FP4, covering 10-600 cm^{-1}, 600-1050 cm^{-1}, and 1050-1430 cm^{-1}, respectively. With all
129 three focal planes, CIRS measures Jupiter's thermal emission in wavenumber over 10 to 1430
130 cm^{-1} (i.e., 7 to 1000 μm) with adjustable spectral resolutions from 0.5 to 15.5 cm^{-1}. In this study,
131 we analyze Jupiter's spectra with two resolutions (i.e., 2.8 cm^{-1} and 0.5 cm^{-1}), that provide the
132 best spatial coverage. Data with other spectral resolutions are not included because their spatial
133 coverage is negligible compared the spectra with resolutions of 2.8 cm^{-1} and 0.5 cm^{-1}.
134
135 Figure 1 displays a typical spectrum of Jupiter recorded by CIRS. The theoretical framework
136 introduced in previous studies (Conrath et al., 1989; Li et al., 2010) shows that the outgoing
137 thermal emission is determined by measurements of outgoing radiance at different emission
138 angles and different latitudes. Therefore, we process the CIRS spectra into 2-dimensional
139 (latitude × emission angle) wavenumber-integrated radiance (Li et al., 2010) with a resolution of
140 1° in both latitude and emission angle. Here, we average all CIRS observations within each 1°
141 latitude bin based on the center latitudes of spectra. The spatial resolution of processed data (1°)

142 is higher than the spatial resolution of the raw CIRS observations (~ 3-40°), which is determined
143 by the field of view of CIRS and the distance between Jupiter and Cassini. Figure 2 shows the
144 final data products: zonal-mean wavenumber-integrated radiance in the plane of latitude and
145 emission angle recorded by FP1, FP3, and FP4, respectively. Figure 2 suggests that Jupiter's
146 radiance varies not only in the direction of latitude about also in the direction of emission angle.
147 The variation of Jupiter's radiance along the direction of longitude is generally less than 3%,
148 which is not shown in Fig. 2, but is accounted in the estimates of the uncertainty of Jupiter's
149 emitted power (please see Section 4).
150
151 **3.2) Cassini/VIMS Observations**
152 The shortest wavelength (i.e., largest wavenumber) of the CIRS spectra is ~ 7 μm (i.e., ~ 1430
153 cm^{-1}). Therefore, the CIRS observations do not record the 5-μm thermal emission spectral
154 component of Jupiter. This range is covered by another Cassini infrared instrument – VIMS. The
155 VIMS instrument is a color camera that acquires spectral cubes encompassing 352 different
156 wavelengths between 0.35 μm and 5.1 μm (Brown et al., 2004). It is designed to measure
157 scattered and emitted light from surfaces and atmospheres, with emphasis on covering a broad
158 spectral domain with moderate spatial resolution.
159
160 In this study, we use 11 full-disk VIMS observations recorded on January 7-8, 2001, about eight
161 days after the closest approach to Jupiter. The VIMS observations from 4.4 μm to 5.1 μm are
162 utilized to explore the emitted power of the 5-μm thermal band, which has a spectral range of
163 4.4-5.6 μm (see Section 4.2). All global VIMS images at different wavelengths are well
164 navigated and calibrated by the VIMS Operations Team based at the University of Arizona,

following techniques discussed by Barnes et al., (2007). The raw 5-μm VIMS global images are generally stored in units of I/F, the ratio of recorded radiance to the known total incident solar radiance (Thekaekara, 1973). Panel A of Fig. 3 displays one example of the 5-μm VIMS global images in such units. With the known total incident solar radiance, we can convert the recorded VIMS radiance from I/F to a general radiance unit (panel B). To obtain the intrinsic thermal emission of Jupiter around 5 μm, we eliminate the solar scattering component by analyzing only the night-side portions of these VIMS images (panel C).

4) RESULTS

4.1) Emitted Power in the Wavenumber Range of CIRS

As is evident in Fig. 2, the CIRS observations do not occupy the whole plane of latitude and emission angle. In order to calculate the emitted power at each latitude from integration of the radiance over the entire range of emission angle (Li et al., 2010), it is necessary to fill the gaps in the observed emission angle. Following the method used in our study of Saturn's emitted power (Li et al., 2010), wherein the interpolation/extrapolation from the existing observations was accomplished with a technique of least-squares fit (Bevington and Robinson, 2003), we fill the observational gaps in FP3 and FP4 (panels B and C). Different polynomials of emission angle were tried for the best fitting (i.e., the fitting with the least fitting residual). Here, the fitting residual is defined as the difference between the fitting value and observational data (i.e., fitting value-observational data). We find that the following first-order (degree) polynomial has the best fitting results for observed radiance by FP3 and FP4:

$$I(\delta) = c_1 \cos\delta + c_2 \quad (1)$$

where δ is emission angle. The parameters c_1 and c_2 are coefficients that are fitted and determined by the observed radiance. Figure 4 shows some example fits with Eq. (1) at different latitudes for the focal planes FP3 and FP4, which suggests that the least-squares fit works well for the existing observations.

The fitting function Eq. (1) with the known coefficients (c_1 and c_2) is used to fill the observational gaps in emission angle for the radiance recorded by FP3 and FP4 (panels B and C in Fig. 2). The radiance after filling the observational gaps is shown in panel A of Figs. 5 and 6. Panel B of Figs. 5 and 6 is the ratio of fitting residual to the raw radiance for these observational points, which highlights the difference between the observations and the fitting results. Panel B shows that the ratio is mostly less than 5% at all latitudes. The fitting residual is further utilized in the following estimates of the uncertainty of filling observational gaps.

However, the same technique does not work for the FP1 observations, because the coverage of observed FP1 radiance is very limited (panel A of Fig. 2). For a planetary atmosphere, the thermal radiances at different wavenumbers are correlated with each other. Such a correlation can be utilized to estimate the radiance at the unmeasured wavenumbers from the radiance at the measured wavenumbers (Ingersoll et al., 1975). Here, we estimate the unmeasured FP1 radiance (10-600 cm^{-1}) from the FP3 radiance (600-1050 cm^{-1}), which has much better spatial coverage.

First, we examine the correlation between the FP1 radiances and the FP3 radiance. Our experiments show that there is good correlation between the FP1 radiances and the FP3 radiances with the each latitude bin. Fig.7 displays the scatter plots for these latitude bins with the

210 relatively more simultaneous observations from FP1 and FP3, which are based on panels A and
211 B of Fig. 2. The good correlation between the FP1 radiances and the FP3 radiances makes it
212 possible to regress the FP1 radiances from the FP3 radiances. Figure 8 shows the ratios of the
213 FP1 radiances to the FP3 radiances (i.e., FP1/FP3). This figure suggests that the ratio FP1/FP3
214 does not vary significantly with emission angle, probably because the FP1 and FP3 radiances
215 have the same variation with emission angle (Fig. 2). Figure 9 further presents the zonal mean
216 value and the standard deviation of FP1/FP3 within each latitude bin in Fig. 8. The ratio of the
217 standard deviation (panel B) to the zonal mean value (panel A) is less than 1.5% (panel C),
218 which indicates that there is no significant variation along the direction of emission angle. Figure
219 8 also shows that there are some banded structures of the radiance ratio FP1/FP3 in the
220 meridional direction. The banded structures in Fig. 8 are correlated to the banded structures in
221 the radiance recorded by FP3 (panel A of Fig. 5), which are further related to the banded
222 structures of clouds on Jupiter.
223
224 The correlation of the banded structures between the ratio FP1/FP3 (Fig. 8) and the FP3 radiance
225 (Fig. 5) can be used to explore the FP1 radiance. Panel A of Fig. 10 shows the zonal mean of the
226 FP3 radiance within each latitude bin, which is based on panel A of Fig. 5. The structures of the
227 FP3 radiance in the meridional direction have similar shape as the structures of the ratio FP1/FP3
228 (panel A of Fig. 9) but with opposite direction, which suggests that the FP3 radiance is dominant
229 in the ratio FP1/FP3. Therefore, we can utilize the linear regression of the FP3 radiance to
230 estimate the ratio FP1/FP3 in these latitudes where the FP1 observations are not available. Panel
231 B of Fig. 10 shows the comparison between the linearly regressed ratio FP1/FP3 and the

232 observed ratio FP1/FP3. The correlation coefficient between the observed FP1/FP3 and the
233 regressed FP1/FP3 is beyond 0.99, which suggests that the linear regression works well.
234
235 Based on the fitting results of the FP3 radiance (panel A of Fig. 5) and the regressed ratio
236 FP1/FP3 (panel B of Fig. 10), we can estimate the FP1 radiance in the plane of latitude and
237 emission angle, which is displayed in panel A of Fig. 11. Panel B of Fig. 11 shows the ratio of
238 the regression residual (i.e., difference between the regressed FP1 radiance and the raw FP1
239 radiance) to the raw FP1 radiance. The ratio in panel B is basically less than 2%, which suggests
240 that the linear regression of the FP3 radiance works well for estimating the FP1 radiance.
241
242 After filling the observational gaps in the thermal radiance recorded by the three CIRS focal
243 planes (panel A of Figs. 5, 6, and 11), we can estimate Jupiter's emitted power. Figure 12 shows
244 the meridional profile of Jupiter's emitted power in the CIRS spectral range (10-1430 cm^{-1} ~ 7-
245 1000 μm). The uncertainties shown in Fig. 12 include three sources: 1) the uncertainty related to
246 the CIRS calibration; 2) the uncertainty related to the filling of observational gaps in the
247 emission angle along the each latitude; and 3) the standard deviation of multiple CIRS
248 observations with different longitudes with the same latitude and emission angle. The first
249 uncertainty source, which is related to the CIRS calibration by removing the radiance of the
250 background, can be estimated by the spectra of deep space (Li et al., 2010). The second
251 uncertainty source is related to the filling of observational gaps in FP1 and FP3/4 by the least-
252 squares fit and the linear regression, respectively. The method of estimating the uncertainties
253 related to the filling of the observational gaps by FP3 and FP4 by the least-squares fit, which is
254 based on the fitting residual (i.e., fitting value-observational data), has been discussed in our

255 previous Saturn paper (Li et al., 2010). Along the each latitude, the standard deviation of the
256 fitting residual at these emission angles with available FP3/FP4 data is used to estimate the
257 uncertainty of the fitting radiances at these emission angles, where the FP3/FP4 raw data are not
258 available (i.e., observational gaps) (Li et al., 2010). As for the uncertainty related to the regressed
259 FP1 radiance by the linear regression of the FP3 radiance, we use the standard deviation of the
260 regression residual (panel B of Fig. 11) to estimate the uncertainty at these latitudes where the
261 FP1 raw data are available. Based on the existing estimates of the FP1 uncertainty, we use a
262 linear interpolation/extrapolation to estimate the FP1 uncertainty in these latitudes where the raw
263 FP1 observations are not available. The second uncertainty, which has a magnitude $10^{-1}Wm^{-2}$, is
264 two-order of magnitude larger than the first uncertainty, which has a magnitude $10^{-3}Wm^{-2}$. The
265 third uncertainty, which is the standard deviation of multiple CIRS measurements at different
266 longitudes with the same latitude and emission angle, has the same magnitude as that of the
267 second uncertainty. Considering that the three uncertainty sources are independent, we combine
268 them by the square root of the sum of the squares of the individual uncertainties (Daley, 1991).
269

270 **4.2) Emitted Power From the 5-μm thermal Emission**

271 We use the VIMS observations to measure Jupiter's emitted power around 5 μm, which is
272 outside of the spectral range of the CIRS spectra. The complete 5-μm thermal emission band
273 covers the spectral range 4.4-5.6 μm (Irwin, 1999), longer than the spectral range of 4.4-5.1 μm
274 covered by VIMS. To derive the power over the full 5-μm thermal band, we fist integrate VIMS
275 spectra over the spectral range of 4.4-5.1 μm. We then explore the ratio of wavelength-integrated
276 radiance between the VIMS spectral range (i.e., 4.4-5.1 μm) and the complete spectral range
277 (i.e., 4.4- 5.6 μm). Finally, the VIMS observations and the radiance ratio between 4.4-5.1 μm

278 and 4.4- 5.6 μm are combined together to estimate the total emitted power from the 5-μm
279 thermal band.
280
281 Our examination (not shown) and the previous study (Roos-Serote and Irwin, 2006) both suggest
282 that the magnitude of Jupiter's 5-μm spectra varies with time and space but the shape of the
283 spectra basically remains unchanged. Therefore, it is reasonable to assume that the ratio of
284 wavelength-integrated radiance between the VIMS spectral range (i.e., 4.4-5.1 μm) and the
285 complete spectral range (i.e., 4.4- 5.6 μm) does not change significantly with time and space on
286 Jupiter. Therefore, we can estimate the total 5-μm thermal emission over 4.4- 5.6 μm from the
287 known VIMS measurements over 4.4-5.1 μm if we know the ratio between them.
288
289 We use the complete 5-μm spectra from the Infrared Interferometer Spectrometer (IRIS) on
290 Voyager to get the ratio of wavelength-integrated radiance between the VIMS spectral range
291 (4.4-5.1 μm) and the complete spectral range (4.4-5.6 μm). Figure 13 shows the comparison of
292 the global-average spectrum between Cassini/VIMS and Voyager/IRIS, which suggests that the
293 5-μm spectra from IRIS and VIMS have basically the same structures. It should be mentioned
294 that some fine spectral structures shown in the IRIS spectrum do not show in the VIMS
295 spectrum, because the spectral resolution is much higher in IRIS (~ 0.005 μm) than in VIMS (~
296 0.017 μm). We use the complete IRIS spectrum to compute the ratio of wavelength-integrated
297 radiance between the VIMS spectral range (i.e., 4.4-5.1 μm) and the complete spectral range
298 (i.e., 4.4- 5.6 μm), which has a value of 0.711.
299

We divide the wavelength-integrated radiance from the VIMS measurements (4.4-5.1 μm) by the ratio to estimate the total emitted power from the thermal emission around 5 μm, which is shown in Fig. 14. The uncertainty (error-bar) shown in Fig. 14 is based on two factors: 1) the absolute calibration error and 2) the standard deviation of multiple VIMS measurements within each latitude bin (1°) and within the two-day period (January 7-8, 2001 with 11 global observations). For the first factor, we refer to the study by Buratti et al., (2010), in which the absolute error of the VIMS data was estimated to be 5-10% of the recorded VIMS radiance. Here, we use the average value (i.e., 7.5%) to represent the absolute calibration error. The second uncertainty factor, which is related to the longitudinal and temporal variation of the 5-μm radiance, can reach ~ 50% of the total 5-μm radiance at some latitudes. Figure 14 shows the strongest 5-μm thermal emission exists in the latitude band around 15° in the two hemispheres. The global-average emitted power of the 5-μm thermal emission is 0.09±0.01 Wm^{-2}, which is ~ 0.7±0.1% of Jupiter's total emitted power ~ 14.10±0.02 Wm^{-2} (see Section 4.3). The strongest 5-μm thermal emission around 15°N can reach ~ 1.9±0.6% of Jupiter's total emitted power at this latitude.

4.3) Total Emitted Power of Jupiter

Thermal radiance outside the spectral range of CIRS (10-1430 cm^{-1}) and the 5-μm emission band (1800-2250 cm^{-1}) has negligible contribution to the total emitted power of Jupiter (Conrath et al., 1989), and so it is not considered in this study. Thus, we estimate Jupiter's emitted power and effective temperature at different latitudes by simply adding the values in Fig. 12 and Fig. 14. The corresponding uncertainty is estimated by the square root of the sum of the squares of the uncertainties from the CIRS measurements (Fig. 12) and the VIMS measurements (Fig. 14), because the two uncertainties are independent (pages 42-43 in Bevington and Robinson, 2003).

323 The meridional distribution of Jupiter's total emitted power is displayed in Fig. 15, which shows
324 an asymmetry of emitted power/effective temperature between the northern and southern
325 hemispheres. There are very limited observations in the polar region beyond 77° in the Jupiter
326 flyby mission by Cassini, so we cannot estimate the emitted power in the polar region. Assuming
327 the emitted power at the unmeasured polar region (77-90° S/N) has the same value and
328 uncertainty as the value at 76° S/N, we can evaluate the hemispheric average of emitted power
329 and the corresponding effective temperature, which are shown in Table 1. Table 1 shows that the
330 emitted power and effective temperature are higher in the northern hemisphere (NH) than in the
331 southern hemisphere (SH) by $0.41\pm0.04 Wm^{-2}$ ($3.0\pm0.3\%$) and $0.92\pm0.09K$ ($0.7\pm0.1\%$),
332 respectively.
333
334 In addition to the asymmetry between the two hemispheres, there are some relatively small-scale
335 oscillations of emitted power/effective temperature shown in Fig. 15, which are related to the
336 temperature structures in Jupiter's troposphere. The tropical temperature shown in this figure
337 was retrieved from the Cassini/CIRS spectra at a wavenumber range of 600-690 cm^{-1} (Flasar et
338 al., 2004b, Simon-Miller et al., 2006). Figure 16 shows that the profile of effective temperature
339 sits between the 330-mbar profile and the 420-mbar profile of atmospheric temperature.
340 Therefore, the weighting function of the outgoing thermal radiance peaks around the two
341 pressure levels. Figure 16 also shows that the structures of effective temperature in the two
342 hemispheres are more similar to the temperature profiles of the shallower atmosphere (170-270
343 mbar), suggesting that they also contribute to Jupiter's outgoing thermal radiance. Figure 16
344 suggests that Jupiter's emitted power (i.e., effective temperature) is related to the atmospheric
345 temperature. However, the asymmetry between the two hemispheres, which is shown in Jupiter's

346 emitted power (Fig. 15), does not significantly show in the atmospheric temperature (Fig. 16).
347 Therefore, we suggest that there are other mechanisms (e.g., spatial distribution of cloud/haze)
348 possibly influencing the meridional distribution of Jupiter's emitted power.
349
350 The meridional distribution of emitted power was also measured in some previous studies
351 (Pirraglia, 1984; Ingersoll, 1990). Pirraglia (1984) measured the meridional profile of emitted
352 power with the flyby observations by Voyager 1. The meridional profile in the paper by Ingersoll
353 (1990) was combined from the Voyager observations in the low and middle latitudes (Pirraglia,
354 1984) and the Pioneer observations in the high latitudes (Ingersoll et al., 1975). There are no
355 multiple focal panels in the Voyager/IRIS (Hanel et al., 1980), and the observations recorded by
356 the Voyager/IRIS have very limited coverage in the plane of latitude and emission angle (Hanel
357 et al., 1981; Pirraglia, 1984). Therefore, the method we used in this study for computing Jupiter's
358 emitted power from the Cassini/CIRS observations (i.e., interpolating the FP3/FP4 observations
359 and regressing the FP1 observations from the FP3/FP4 observations) does not work for the
360 Voyager/IRIS observations. Instead, a method, in which the gaps in the emission angle are
361 considered by the radiative-transfer calculations with the given atmospheric temperature and
362 opacity profiles (Hanel et al., 1981, 1983), was used in the analysis of the Voyager observations
363 (Pirraglia, 1984; Ingersoll et al., 1990). The comparison between the limited observations and the
364 radiative-transfer calculations (Pirraglia, 1984) suggests that the above method also works well
365 under the condition of lacking the necessary coverage of latitude and emission angle.
366
367 Figure 17 displays the profile of emitted power from the Voyager observations in 1979,
368 compared to the profile from the Cassini observations in 2000-01. The uncertainty in the

369 Voyager profile comes from the measurements by Pirraglia (1984). In the study by Pirraglia
370 (1984), the standard deviation of multiple measurements within each latitude bin, corresponding
371 to the zonal mean emitted power along the longitude direction, was taken as the uncertainty.
372 Such an estimate of uncertainty does not account for the uncertainty related to the calibration of
373 the Voyager/IRIS, which has a magnitude $10^{-2}Wm^{-2}$ (Hanel et al., 1981). However, the
374 uncertainty due to the calibration is approximately one-order of magnitude smaller than the
375 standard deviation shown in Fig. 17 ($\sim 10^{-1}Wm^{-2}$). Therefore, it does not significantly vary the
376 uncertainty estimated by Pirraglia (1984). The uncertainty of the Cassini profile is based on more
377 uncertainty sources from the CIRS measurements (Section 4.1) and the VIMS measurements
378 (section 4.2). The latitude bin in the Cassini measurements (i.e., 1°) is narrower than the latitude
379 bin in the Voyager/IRIS measurements (i.e., 4-5°) (Pirraglia, 1984). The standard deviation of
380 multiple measurements within each latitude bin in the previous study (Pirraglia, 1984) is roughly
381 three times of that in our study. Figure 17 shows that the total uncertainty considering more
382 sources in our study is still smaller than the uncertainty in the Voyager measurements by
383 Pirraglia (1984).
384
385 Figure 17 shows significant difference between the two profiles, which is larger than the
386 measurement uncertainty at most latitudes. In particular, the asymmetry of emitted
387 power/effective temperature between the two hemispheres, which is evident in the Cassini
388 observations, does not appear in the Voyager measurements. Table 2 shows the comparison of
389 global-average emitted power and effective temperature between the current measurements by
390 Cassini and the previous measurements by Voyager 1 (Hanel et al., 1981). In addition, the
391 global-average value from the measurements by Pioneer (Ingersoll et al., 1975), which have

392 relatively larger uncertainty, is also listed in Table 2. The differences of emitted power and
393 effective temperature between Voyager and Cassini are larger than the corresponding
394 uncertainties. From the Voyager epoch to the Cassini epoch, the global-average emitted power
395 and effective temperature increased by $0.51\pm0.14 Wm^{-2}$ (3.8±1.0%) and 1.17±0.31 K (0.9±0.2%),
396 respectively. When exploring the temporal variation of the global values between the two
397 epochs, the known uncertainty sources including data calibration are considered in the
398 measurements by Voyager (Hanel et al., 1981) and by Cassini (this study). It should be
399 mentioned that it is still possible that there are unknown calibration issues affecting the
400 measurements in the two epochs.
401
402 Why did Jupiter's emitted power and effective temperature change with time? We first examine
403 if there is any variation in the altitude of the atmospheric layers involving the outgoing thermal
404 radiance on Jupiter. Figure 18 displays the comparison of the effective temperature and the
405 atmospheric temperature in the Voyager epoch. The tropospheric temperature shown in Fig. 18
406 comes from the retrievals of the Voyager/IRIS spectra in the spectral intervals 320-430 cm^{-1} and
407 520-600 cm^{-1} (Simon-Miller et al., 2006). The comparison shows that the profile of effective
408 temperature sits between the 310-mbar profile and 410-mbar profile of atmospheric temperature,
409 which suggests that the atmospheric layers around the two pressure levels contribute
410 significantly to the outgoing thermal radiance on Jupiter. The difference between the profile of
411 effective temperature and the profiles of atmospheric temperature at 310 mbar and 410 mbar
412 suggests that the atmospheric layers at other pressure levels also contribute to Jupiter's outgoing
413 thermal radiance. The comparison between Fig. 16 (Cassini profiles) and Fig. 18 (Voyager
414 profiles) further suggests that the peak of the weighting function of the outgoing thermal

415 radiance did not change significantly from the Voyager epoch to the Cassini epoch. Therefore,
416 we rule out the varying weighting function of outgoing thermal radiance as the main physics
417 behind the temporal variation of emitted power/effective temperature shown in Fig. 17.
418
419 Jupiter's emitted power is directly related to the temperature of atmospheric layers, so the
420 temporal variation of emitted power (Fig. 17) means that there is the corresponding variation in
421 the atmosphere temperature. Figure 19 is the comparison of Jupiter's temperature in the upper
422 troposphere between the Voyager epoch and the Cassini epoch. Figure 19 suggests that the
423 warming of the atmospheric layers around 200 mbar contributes to the increased emitted power
424 in the latitude bands outside of the equatorial region (i.e., 10°N-10°S) (Fig. 17). In addition, the
425 cooling of the atmospheric layers between 50 mbar and 500 mbar in the equatorial region
426 explains the decreased emitted power in that region from the Voyager epoch to the Cassini
427 epoch. Much of this cooling was noted immediately after the Voyager encounters (Orton et al.,
428 1994) and was even detectable between Voyagers 1 and 2.
429
430 The temporal variation of the atmospheric temperature provides one explanation for the varied
431 emitted power from Voyager to Cassini. The continuous observations from 1980 to 1993 (Orton
432 et al., 1994) and from 1979 to 2001 (Simon-Miller et al., 2006) suggest that Jupiter's
433 tropospheric temperature changed gradually from the Voyager epoch to the Cassini epoch (i.e., ~
434 2 Jovian years), with little obvious seasonal or short-term variation. In other words, there is
435 probably long-term variation (e.g., inter-annual variation) in Jupiter's tropospheric temperature.
436 As a result, Jupiter's emitted power and effective temperature, which are mainly determined by

437 Jupiter's tropospheric temperature, probably have a corresponding inter-annual variability
438 existing in the temporal variation shown in Fig. 18.
439
440 Next, we explore the physics behind the temporal variation of the atmospheric temperature and
441 hence the emitted power from the Voyager epoch to the Cassini epoch. First, let us take a look at
442 the solar flux on Jupiter. The average solar longitude of the Voyager observations was 174.5°.
443 The average solar longitude of the Cassini mission in 2000-01 was 110.5°. Figure 20 shows the
444 seasonal variation of solar flux from the Voyager epoch (i.e., solar longitude ~ 174.5°; northern
445 late summer) to the Cassini epoch (i.e., solar longitude ~ 110.5°; northern early summer). On
446 Earth, the temporal variation in the meridional distribution of solar flux is the main driver of the
447 seasonal variation of atmospheric temperature. However, the temporal variation in the
448 meridional distribution of solar flux (Fig. 19) is probably not the main driver for the temporal
449 variation of atmospheric temperature (Fig. 18), mainly because of the relativity small temporal
450 variation of solar flux on Jupiter due to its small orbital obliquity (i.e., 3°). The comparison
451 between Fig. 19 and Fig. 20 also suggests that there is no direct relationship between the varying
452 solar flux and the temporal variation of atmospheric temperature. First, the increased solar flux in
453 the NH cannot explain the cooling of atmospheric temperature between 50 mbar and 100 mbar
454 (Fig. 19). Second, the decreased solar flux in the high latitudes of the SH cannot explain the
455 increased atmospheric temperature around 200 mbar in the same latitudes. Finally, the smooth
456 profile of solar flux and its temporal variation cannot explain the temporal variation of
457 atmospheric temperature at the small length-scale (i.e., a few latitude degrees) in Fig. 19.
458 Therefore, the above analyses suggest that there are probably other mechanisms to drive the

459 temporal variation of tropospheric temperature, emitted power, and effective temperature on
460 Jupiter.
461
462 The second possible driving force is the decadal-scale variability of cloud cover on Jupiter
463 (Baines et al., 2007). The variation of cloud cover will redistribute the solar flux on Jupiter, and
464 hence modify the thermal structure and the related emitted power. The third possible driving
465 force is wave activity. The atmospheric waves, which are thought to be the mechanism of the
466 Quasi-Biennial Oscillation (Lindzen and Holton, 1968, Baldwin et al., 2001) and sudden
467 warming (Baldwin and Dunkerton, 1989) in the stratosphere of Earth, can also drive the large-
468 scale variation of temperature and wind fields. Likewise, such a mechanism works for the quasi-
469 quadrennial oscillation on Jupiter (Leovy et al., 1991; Orton et al., 1991; Friedson et al., 1999; Li
470 and Read, 2000). The wave-driven oscillations mainly exist in the stratospheres of planetary
471 atmospheres, but we cannot rule out the roles of waves (Porco et al., 2003; Li et al., 2006) and
472 other dynamical processes (e.g., vortices, eddies and storms) in modifying the large-scale
473 thermal structure in the troposphere of Jupiter.
474
475 **5) CONCLUSION AND DISCUSSION**
476 Jupiter's spectra recorded by Cassini CIRS and VIMS during the period of 2000-01 are
477 systematically analyzed to evaluate the emitted power and effective temperature of Jupiter. Our
478 analysis indicates that in the Cassini epoch the global-average emitted power and effective
479 temperature were 14.10±0.03 Wm^{-2} and 125.57±0.07 K, respectively. Jupiter's 5-μm thermal
480 emission, which is produced near the 6-bar level and is modulated by relatively deep cloud layers
481 of ammonia hydrosulfide (i.e., ~ 1-3 bar), contributes ~ 0.7±0.1% to the total emitted power at

482 the global scale. However, the strongest 5-μm thermal emission around 15°N can reach ~
483 1.9±0.6% of the total emitted power at that latitude. The emitted power was 3.0±0.3% higher in
484 the NH than in the SH in the Cassini epoch. Such an asymmetry was not present in the Voyager
485 epoch. Furthermore, Jupiter's emitted power increased ~ 3.8±1.0% on a global scale from the
486 Voyager epoch to the Cassini epoch.
487
488 Our analyses of atmospheric temperature reveal that the temporal variation of emitted power
489 from the Voyager epoch to the Cassini epoch is mainly due to the warming of atmospheric layers
490 around 200 mbar. The mechanisms of the temporal variation of tropopheric temperature and the
491 related emitted power are unclear. We suggest that the temporal variation of cloud cover and
492 some dynamical processes (e.g., waves, vortices, eddies, and storms) are possible mechanisms to
493 drive the temporal variation of the large-scale atmospheric temperature and hence the temporal
494 variation of emitted power on Jupiter, but long-term continuous observations and more
495 theoretical studies are needed to understand the temporal variation in the jovian atmosphere. On
496 the other hand, the varying emitted power implies that the energy budget and its meridional
497 distribution probably change with time on Jupiter. The potentially varying energy budget will
498 inversely modify the atmospheric structures, large-scale circulation, and dynamical processes.
499 Therefore, the coupling between the varying energy budget and the evolving atmospheric
500 structure/dynamics, which makes Jupiter's atmospheric system very complicated, should be
501 considered in the future exploration.
502
503 Our follow-up studies, which are based on observations of reflected solar radiance in the visible
504 band from the Imaging Science Subsystem (ISS) and VIMS on Cassini, will help us measure the

absorbed solar radiance on Jupiter during the Cassini epoch. Combining measurements of the emitted thermal radiance and absorbed solar energy, we can determine the energy budget and hence internal heat in the Cassini epoch. As well, Cassini measurements can be compared with previous measurements (i.e., Pioneer and Voyager) to detect and characterize the temporal variation of the energy budget and internal heat on Jupiter.

528 **References**

529

530 Baines, K. H., and 18 colleagues, 2007. Polar lightning and decadal-scale cloud variability on
531 Jupiter, Science 318, 226-229.

532

533 Barnes, J. W., R. H. Brown, L. Soderblom, B. J. Buratti, C. Sotin, S. Rodriguez, S. L. Mouelic,
534 K. H. Baines, R. Clark, P. Nicholson, 2007. Global-scale surface spectral variation on Titan seen
535 from Cassini/VIMS. Icarus 186, 242-258.

536

537 Baldwin and Dunkerton, 1989. The stratospheric major warming of early December 1987. J.
538 Atmos. Sci. 46, 2863-2884.

539

540 Baldwin, M. P., and 14 colleagues, 2001. The quasi-biennial oscillation. *Reviews of Geophysics*
541 39, 179-229.

542

543 Bevington, P. R., and D. K. Robinson, 2003. Data reduction and error analysis for the physical
544 sciences, third edition. McGraw-Hill, New York.

545

546 Brown, R. H., and 20 colleagues, 2004. The Cassini visual and infrared mapping spectrometer
547 (VIMS) investigation, Space Sci. Rev. 115, 111-168.

548

549 Buratti, B. J., J. M. Bauer, M. D. Hicks, J. A. Mosher, G. Filacchione, T. Momary, K. H. Baines,
550 R. H. Brown, R. N. Clark, P. D. Nicholson, 2010. Cassini spectra and photometry 0.25-5.1 μm of
551 the small inner satellites of Saturn. Icarus 206, 524-536.
552
553 Conrath, B. J., R. A. Hanel, R. E. Samuelson, 1989. Thermal Structure and Heat Balance of the
554 Outer Planets. In Origin and Evolution of Planetary and Satellite Atmospheres edited by Atreya,
555 S. K., J. B. Pollack, and M. S. Matthews, The University of Arizona Press, Arizona.
556
557 Daley, R., 1991. Atmospheric data analysis. Cambridge University Press, Cambridge.
558
559 Flasar, F. M., 1973. Gravitational energy sources in Jupiter. Astrophys. J. 186, 1097-1106.
560
561 Flasar, F. M., and 45 colleagues, 2004a. Exploring the Saturn system in the thermal infrared: The
562 Composite Infrared Spectrometer. Space Sci. Rev. 115, 169–297.
563
564 Flasar, F. M., and 39 colleagues, 2004b. An intense stratospheric jet on Jupiter. Nature 427, 132-
565 135.
566
567 Friedson, A.J., 1999. New observations and modeling of a QBO-like oscillation in Jupiter's
568 stratosphere. Icarus 137, 34–55.
569
570 Friedson, J., A. P. Ingersoll, 1987. Seasonal meridional energy balance and thermal structure of
571 the atmosphere of Uranus: a radiative-convective-dynamical model. Icarus 69, 135-156.

572

573 Gierasch, P. J., A. P. Ingersoll, D. Banfield, S. P. Ewald, P. Helfenstein, A. Simon-Miller, A.
574 Vasavada, H. H. Breneman, D. A. Senske, and Galileo Imaging Team, 2000. Observation of
575 moist convection in Jupiter's atmosphere. Nature 403, 628-630.

576

577 Grossman, A. S., J.B. Pollack, R. T. Reynolds, A. L. Summers, 1980. The effect of dense cores
578 on the structure and evolution of Jupiter and Saturn. *Icarus* 42, 358-379.

579

580 Guillot, T., D. J. Stevenson, W. B. Hubbard, and D. Saumon, 2004. The Interior of Jupiter. In
581 Jupiter: The planet, Satellites, and Magnetosphere edited by Bagenal, F., T. Dowling, and W.
582 Mckinnon, Cambridge University Press, Cambridge.

583

584 Hanel, R. A., B. J. Conrath, L. W. Herath, V. G. Kunde, J. A. Pirraglia, 1981. Albedo, internal
585 heat, and energy-balance of Jupiter – preliminary results of the Voyager infrared investigation. J.
586 Geophy. Res. 86, 8705-8712.

587

588 Hanel, R. A., Conrath, B. J., Jennings, D. E., Samuelson, R. E, 2003. Exploration of the solar
589 system by Infrared Remote Sensing. Cambridge University Press, New York.

590

591 Ingersoll, A. P., G. Munch, G. Neugebauer, D. J. Dineer, G. S. Orton, B. Schupler, M.
592 Schroeder, S. C. Chase, R. D. Ruiz, L. M. Trafton, 1975. Pioneer 11 infrared radiometer
593 experiment – global heat balance of Jupiter. Science 188, 472-473.

594

595 Ingersoll, A. P., 1990. Atmospheric dynamics of the outer planets. Science 248, 308-315.
596
597 Ingersoll, A. P., P. J. Gierasch, D. Banfield and A. R. Vasavada 2000. Moist convection as an
598 energy source for the large-scale motions in Jupiter's atmosphere. Nature 403, 630-632.
599
600 Irwin, P. G. J., 1999. Cloud structure and composition of Jupiter's atmosphere. Surveys in
601 Geophysics 20, 505-535.
602
603 Irwin, P.G.J., A. L. Weir, S. E. Smith, F. W. Taylor, A. L. Lambert, S. B. Calcutt, P. G.
604 Cameron-Smith, R. W. Carlson, K. Baines, G. S. Orton, P. Drossart, T. Encrenaz, and M. Roos-
605 Serote, 1998. Cloud structure and atmospheric composition of Jupiter retrieved from Galileo
606 real-time spectra. *J. Geophys. Res.* **103**, 23,001–23,021.
607
608 Leovy, C.B., A. J. Friedson, G. S. Orton, 1991. The quasi-quadrennial oscillation of Jupiter's
609 equatorial stratosphere. Nature 354, 380-382.
610
611 Li L., A. P. Ingersoll, A. R. Vasavada, A. A. Simon-Miller, R. K. Achterberg, S. P. Ewald, U. A.
612 Dyudina, C. C. Porco, R. A. West, F. M. Flasar, 2006. Waves in Jupiter's atmosphere observed
613 by the Cassini ISS and CIRS instruments, Icarus 185, 416-419.
614
615 Li, L., B. J. Conrath, P. J. Gierasch, R. K. Achterberg, C. A. Nixon, A. A. Simon-Miller, F. M.
616 Flasar, D. Banfield, K. H. Baines, R. A. west, A. P. Ingersoll, A. R. Vasavada, A. D. Del Genio,
617 C. C. Porco, A. A. Mamoutkine, M. E. Segura, G. L. Bjoraker, G. S. Orton, L. N. Fletcher, P. G.

618 J. Irwin, P. L. Read, 2010. Emitted power of Saturn. Journal of Geophysical Research - Planet,
619 115, art. No. E11002. With NASA feature story titled "Saturn is on a cosmic dimmer switch".
620
621 Li, X., P. L. Read, 2000. A mechanistic model of the quasi-quadrennial oscillation in Jupiter's
622 stratosphere. Planet. Space Sci. 48, 637– 669.
623
624 Lindzen, R. S., and J. R. Holton, 1968. A theory of quasi-biennial oscillation, J. Atmos. Sci. 25,
625 1095-1107.
626
627 Marcus, P. S., 2004. Prediction of a global climate change on Jupiter. Nature 428, 828-831.
628
629 Orton, G., A. Friedson, J. Caldwell, H. Hammel, K. Baines, J. Bergstrahl, T. Martin, M.
630 Malcolm, R. West, W. Golisch, D. Griep, C. Kaminski, A. Tokunaga, R. Baron, M. Shure, 1991.
631 Thermal maps of Jupiter: Spatial organization and time dependence of stratospheric
632 temperatures, 1980–1991. Science 252, 537–542.
633
634 Orton, G. S., and 18 colleagues, 1994. Spatial organization and time dependence of Jupiter's
635 tropospheric temperatures, 1980-1993. Science 265, 625-631.
636
637 Perez-Hoyos, S., A. Sanchez-Lavega, 2006. Solar flux in Saturn's atmosphere: penetration and
638 heating rates in the aerosol and cloud laygers. Icarus 180, 368-278.
639
640 Pirraglia, J. A., 1984. Meridional energy balance of Jupiter. Icarus 59, 169-176.

641

642 Porco, C., and 23 co-authors, 2003. Cassini imaging of Jupiter's atmosphere, satellites, and rings.
643 Science 299, 1541–1547.

644

645 Porco, C. C., and 19 colleagues, 2004. Cassini Imaging Science: Instrument characteristics and
646 anticipated scientific investigations at Saturn, Space Sci. Rev. 115, 363-497.

647

648 Roos-Serote, M. P. G. J. Irwin, 2006. Scattering properties and location of the jovian 5-micron
649 absorber from Galileo/NIMS limb-darkening observations. Journal of Quantitative Spectroscopy
650 and Radiative Transfer 101, 448-461.

651

652 Salpeter, E., 1973. On convection and gravitational layering in Jupiter and stars of low mass.
653 Astrophys. J. 181, L83-L86.

654

655 Simon-Miller, A. A., B. J. Conrath, P. J. Gierasch, G. S. Orton, R. K. Achterberg, F. M. Flasar,
656 B. M. Fisher, 2006. Jupiter's atmospheric temperatures: from Voyager IRIS to Cassini CIRS.
657 Icarus 180, 98-112.

658

659 Smoluchowski, R., 1967. Internal structure and energy emission of Jupiter. Nature 215, 691-695.

660

661 Stevenson, D. J., and E. E. Salpeter, 1977. The dynamics and helium distributions in hydrogen-
662 helium planets. Astrophys. J. Suppl. 35, 239-261.

663

664 Thekaekara, M. P., 1973. Solar energy outside the Earth's atmosphere. Solar Energy 14, 109-
665 127.
666
667 Westphal, J. A., 1969. Observations of localized 5-mircron radiation from Jupiter. The
668 Astrophysical Journal 157, L63-L64.
669
670
671
672
673
674
675
676
677
678
679
680
681
682
683
684
685
686

687

688

689 **Figure Captions**

690

691 Figure 1. Jupiter's combined spectrum based on the three spectra obtained by FP1, FP3, and
692 FP4. The combined spectrum, which was recorded at a spectral resolution of 0.5 cm^{-1}, is a mean
693 spectrum averaged over latitudes 10°S - 10°N and over emission angle 20° - 30°. (A) CIRS
694 radiance. (B) Corresponding brightness temperature.

695

696 Figure 2. Coverage of wavenumber-integrated CIRS radiance in the plane of latitude and
697 emission angle. (A) FP1. (B) FP3. (C) FP4. The limited coverage of FP1 is due to its large field
698 of view with respect to FP3 and FP4.

699

700 Figure 3. VIMS maps at 5 μm. (A) Map with unit of I/F. (B) Map with unit of radiance. (C)
701 Night-side map with unit of radiance. The emission angle increases from ~ 0° at the center of
702 disk to ~ 90° at the limb of disk. The spatial resolution of the VIMS maps is ~ 3° in both latitude
703 and longitude.

704

705 Figure 4. Least-squares fitting of the CIRS observations by the focal planes FP3 and FP4 at
706 different latitudes. The red dots are observations, and the blue lines are fitted lines. Panels (A),
707 (B), (C), (D), and (E) are fits for the FP3 observations at 60°N, 30°N, 0°, 30°S, and 60°S,
708 respectively. Panels (F), (G), (H), (I), and (J) are same as (A), (B), (C), (D), and (E) except for
709 the FP4 observations.

710

711 Figure 5. Filling the FP3 observational gaps (panel B of Fig. 2) with the
712 interpolation/extrapolation by the least-squares fit. (A) Raw FP3 radiance and the fitted data. (B)
713 Ratio of fitted residual to the raw observational data.

714

715 Figure 6. Same as Fig. 5 except for the FP4 radiance.

716

717 Figure 7. Scatter plots of the FP1 radiances and the FP3 radiances. Only these latitude bins with
718 the number of the simultaneous FP1 and FP3 observations more than 10 are shown. Panels (A),
719 (B), (C), (D), (E), (F), (G), (H), and (I) are for the observations at 10°N, 9°N, 8°N, 7°N, 6°N,
720 3°N, 1°N, 4°S, and 5°S, respectively.

721

722 Figure 8. Ratio of wavenumber-integrated radiance between FP1 and FP3 (FP1/FP3). The plot is
723 for the overlap areas observed by both FP1 and FP3.

724

725 Figure 9. Zonal mean and standard deviation of the radiance ratio FP1/FP3. The zonal mean and
726 standard deviation are along the direction of emission angle, which is based on the plane of
727 latitude and emission angle shown in Fig. 7. (A) Zonal mean of the ratio; (B) Standard deviation
728 (std) of the ratio; and (C) Ratio of standard deviation to zonal mean.

729

730 Figure 10. Zonal mean of FP3 radiance and the comparison between the observed ratio FP1/FP3
731 and the regressed ratio FP1/FP3. (A) Zonal mean of the FP3 radiance. The zonal mean of the

FP3 radiance is along the direction of emission angle, which is based on the panel A of Fig. 5. (B) Comparison of the ratio FP1/FP3 between the regression and the observation.

Figure 11. Filling the FP1 observational gaps by the linear regression of the FP3 radiance. (A) Raw FP1 radiance and regressed FP1 data. The regressed FP1 data are based on the FP3 radiance (panel A of Fig. 5) and the regressed ratio FP1/FP3 (panel B of Fig. 9). (B) Ratio of the regression residual to the raw observational data.

Figure 12. Meridional profile of the emitted power in the wavenumber range of Cassini/CIRS (10-1430 cm^{-i}). The solid line is the profile of emitted power. The stippling represents the uncertainty of emitted power, which includes different uncertainty sources from the calibration, the filling of the observational gaps, and the variation of Jupiter's radiance along the longitude.

Figure 13. Comparison of the global-average 5-μm spectra between Voyager/IRIS and Cassini/VIMS. The spectral resolutions are ~ 0.005μm and ~ 0.017μm for Voyager/IRIS and Cassini/VIMS, respectively.

Figure 14. Meridional profile of the emitted power from the 5-μm thermal band (1800-2250 cm^{-1} ~ 4.4-5.6 μm). The solid line is the profile of emitted power, and the stippling represents the uncertainty of measurements.

753 Figure 15. Meridional profile of Jupiter's emitted power and effective temperature. The solid line
754 is the profile of emitted power and effective temperature, and the stippling represents the
755 uncertainty of measurements.
756
757 Figure 16. Comparison between the effective temperature and the atmospheric temperature in the
758 Cassini epoch. The red line is Jupiter's effective temperature during the period of October, 2000
759 – March, 2001. The blue lines are the atmospheric temperatures of Jupiter in the roughly same
760 period (Simon-Miller et al., 2006).
761
762 Figure 17. Comparison of meridional profile of the emitted power and effective temperature
763 between the Voyager epoch and the Cassini epoch. The Voyager profile is mainly based on the
764 Voyager observations in 1979 (Pirraglia, 1984). The Voyager profile in the high latitudes comes
765 from the Pioneer observations (Ingersoll et al., 1975, Ingersoll, 1990). The uncertainty of the
766 Voyager profile comes from the estimates by Pirraglia (1984). The Cassini profile comes from
767 Fig. 14.
768
769 Figure 18. Comparison between the effective temperature and the atmospheric temperature in the
770 Voyager epoch. The profile of Jupiter's effective temperature (i.e., red line) comes from Fig. 16.
771 The profiles of Jupiter's atmospheric temperature (i.e., blue lines) comes from a previous study
772 by Simon-Miller et al. (2006).
773
774 Figure 19. Temporal variation of the atmospheric temperature from the Voyager epoch to the
775 Cassini epoch as a function of atmospheric pressure and latitude. There is no available

776 Cassini/CIRS retrieved temperature for the atmospheric layers deeper than 430 mbar due to the
777 limitation of the content information in Jupiter's spectra.
778
779 Figure 20. Comparion of solar flux at the top of Jupiter's atmosphere between the Voyager epoch
780 and the Cassini epoch. The meridional profile of solar flux is determined by the four factors (i.e.,
781 obliquity, eccentricity, incidence angle, and incidence time). The effects due to rings' shadowing
782 and Jupiter's precession are too small to be considered in the computation.
783
784
785
786
787
788
789
790
791
792
793
794
795
796
797
798
799
800
801
802
803
804
805
806
807
808
809
810
811
812

Table 1 Hemispheric average of the emitted power and effective temperature of Jupiter during the Cassini epoch (i.e., 2000-01).

	NH average	SH average
Emitted power (W/m^2)	14.30	13.89
Uncertainty (W/m^2)	± 0.03	± 0.02
Effective temperature (K)	126.03	125.11
Uncertainty (K)	±0.07	±0.05

Table 2 Global-average values of emitted power and effective temperature by Pioneer, Voyager, and Cassini.

	Pioneer 10/11	**Voyager 1**	**Cassini**
Time	December, 1973 and December, 1974	March, 1979	October, 2000 to March, 2001
Solar longitude	16.8°	169.5°	110.5°
Subsolar latitude	0.6°N	0.5°N	2.9°N
Emitted power (W/m^2)	13.8	13.59	14.10
Uncertainty (W/m^2)	± 1.4	± 0.14	± 0.02
Effective temperature (K)	125	124.4	125.57
Uncertainty (K)	±3	±0.3	±0.05

Note: The global values of Pioneer come from the study by Ingersoll et al. (1975). The global values of Voyager 1 come from the study by Hanel et al. (1981).

Figure 1

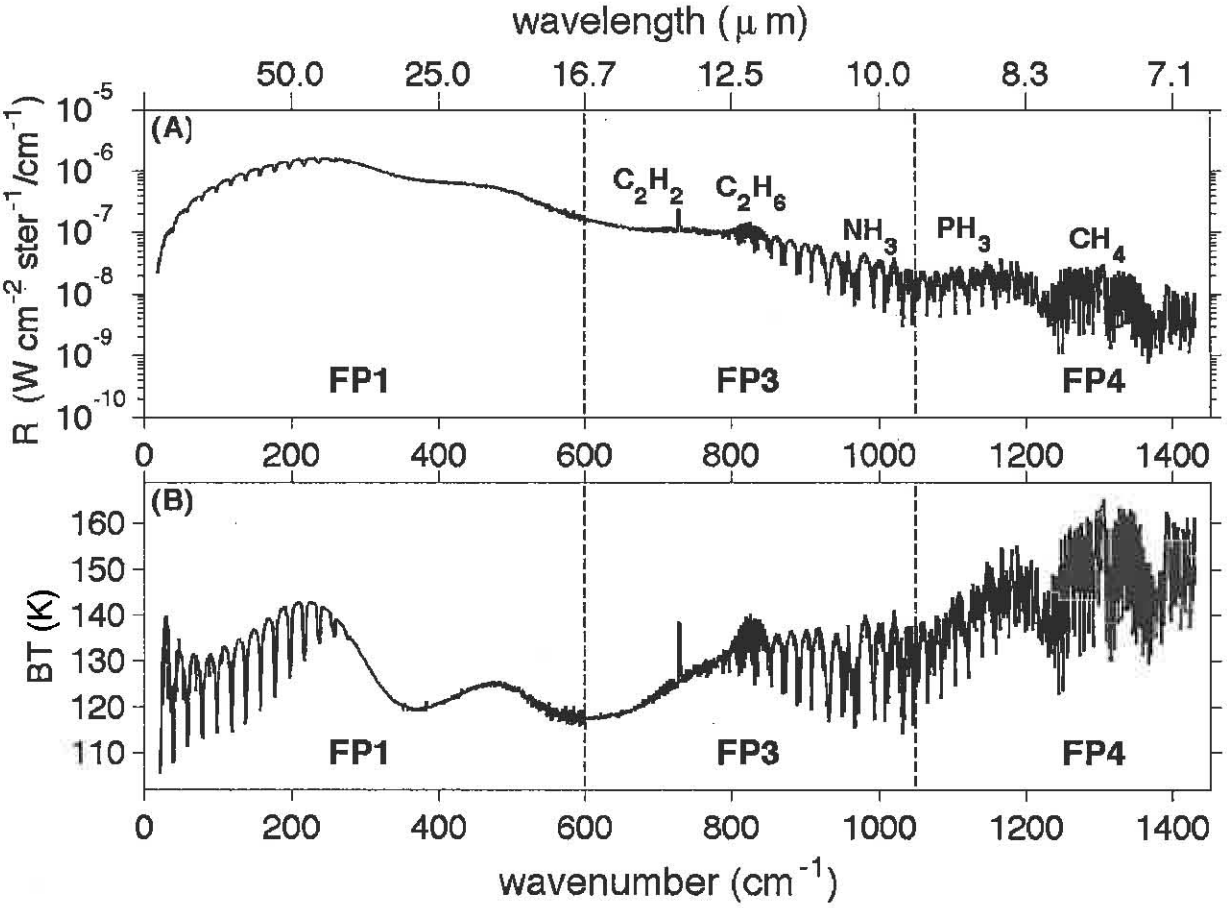
wavelength (μ m)
50.0
25.0
16.7
12.5
10.0
8.3
7.1
(A)
R (W cm-2 ster-1/cm-1)
10-5
10-6
10-7
10-8
10-9
10-10
C2H2
C2H6
NH3
PH3
CH4
FP1
FP3
FP4
0
200
400
600
800
1000
1200
1400
(B)
BT (K)
160
150
140
130
120
110
FP1
FP3
FP4
0
200
400
600
800
1000
1200
1400
wavenumber (cm-1)

Figure 2

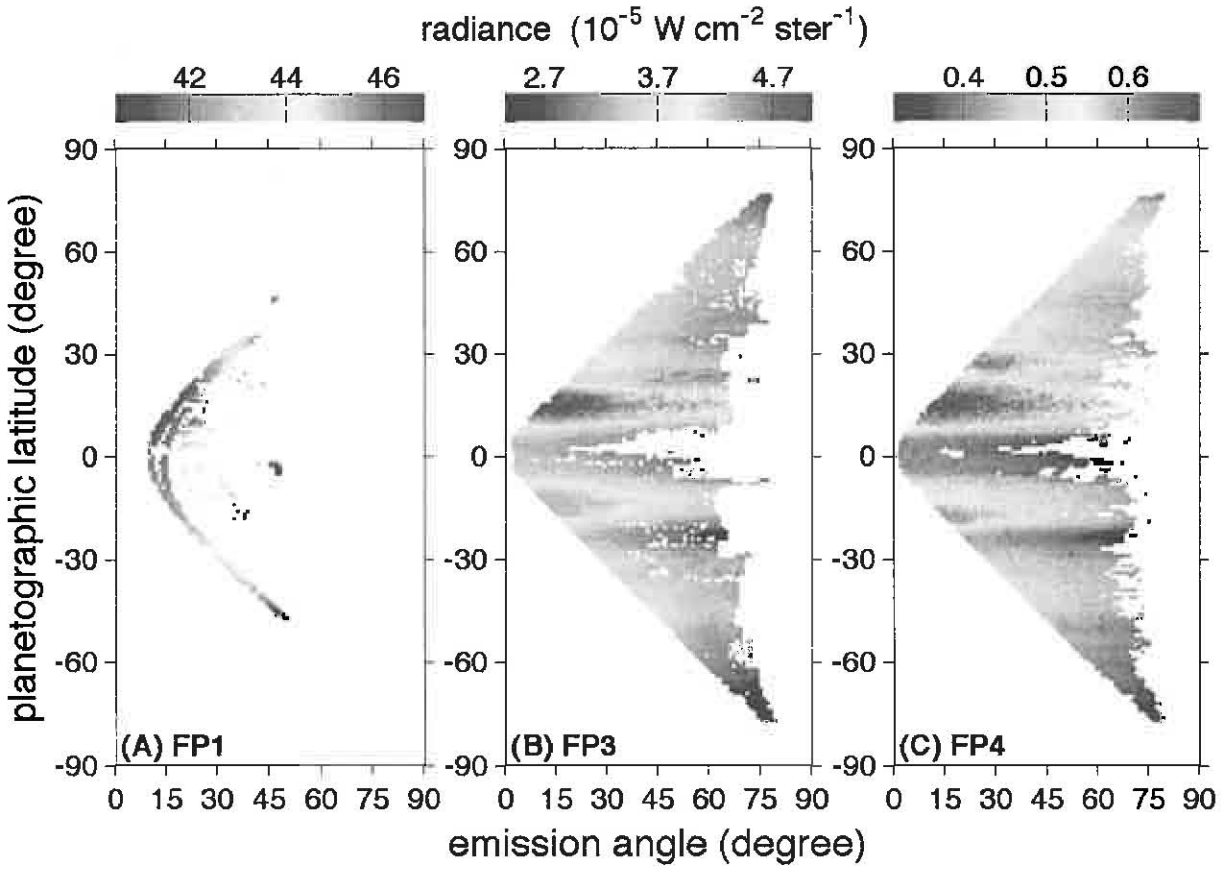
radiance (10^{-5} W cm^{-2} ster^{-1})
42 44 46
2.7 3.7 4.7
0.4 0.5 0.6
planetographic latitude (degree)
90 60 30 0 -30 -60 -90
(A) FP1
(B) FP3
(C) FP4
0 15 30 45 60 75 90
emission angle (degree)

Figure 3

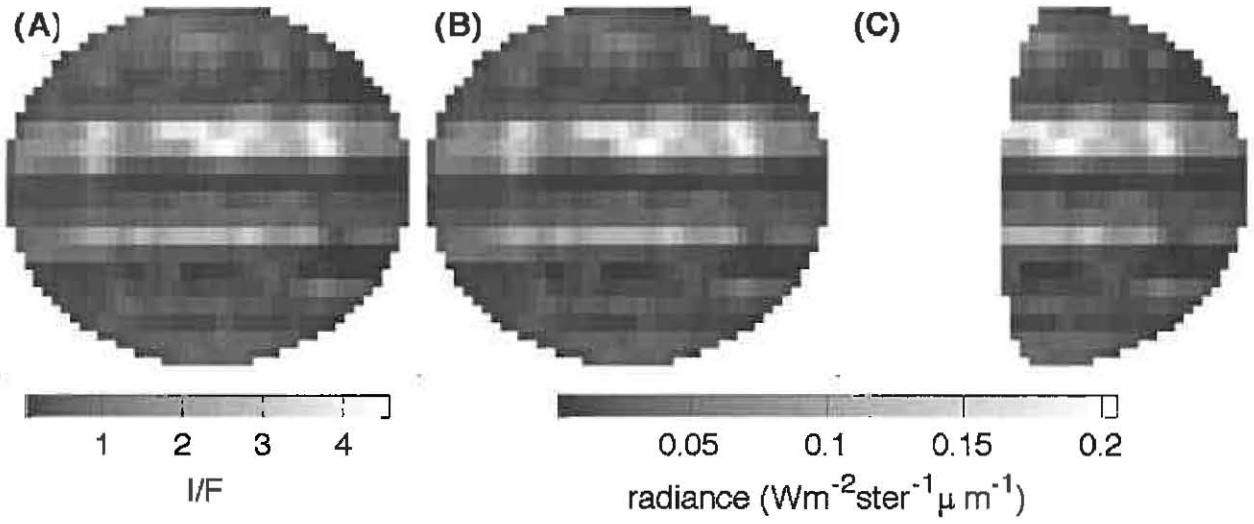

Figure 4

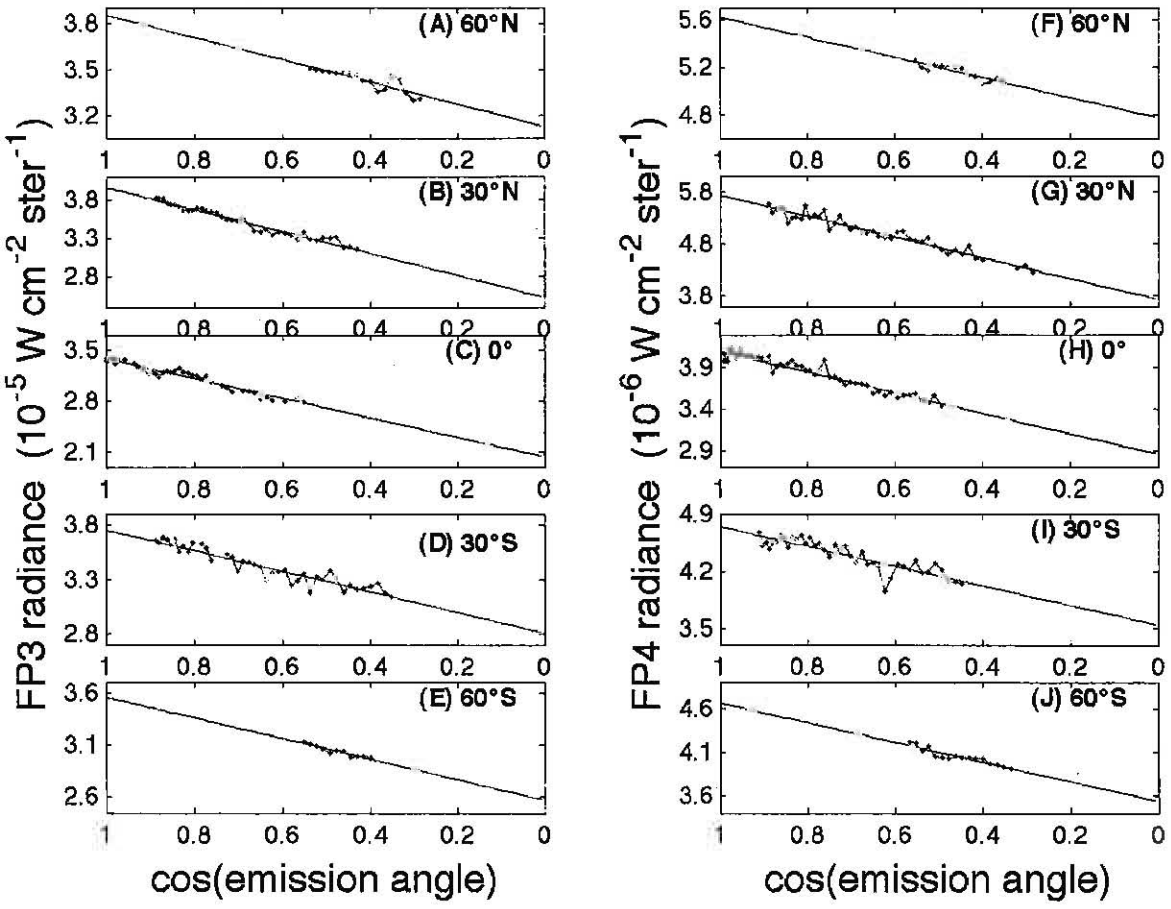
(A) 60°N
(B) 30°N
(C) 0°
(D) 30°S
(E) 60°S
(F) 60°N
(G) 30°N
(H) 0°
(I) 30°S
(J) 60°S
FP3 radiance (10^-5 W cm^-2 ster^-1)
FP4 radiance (10^-6 W cm^-2 ster^-1)
cos(emission angle)
cos(emission angle)

Figure 5

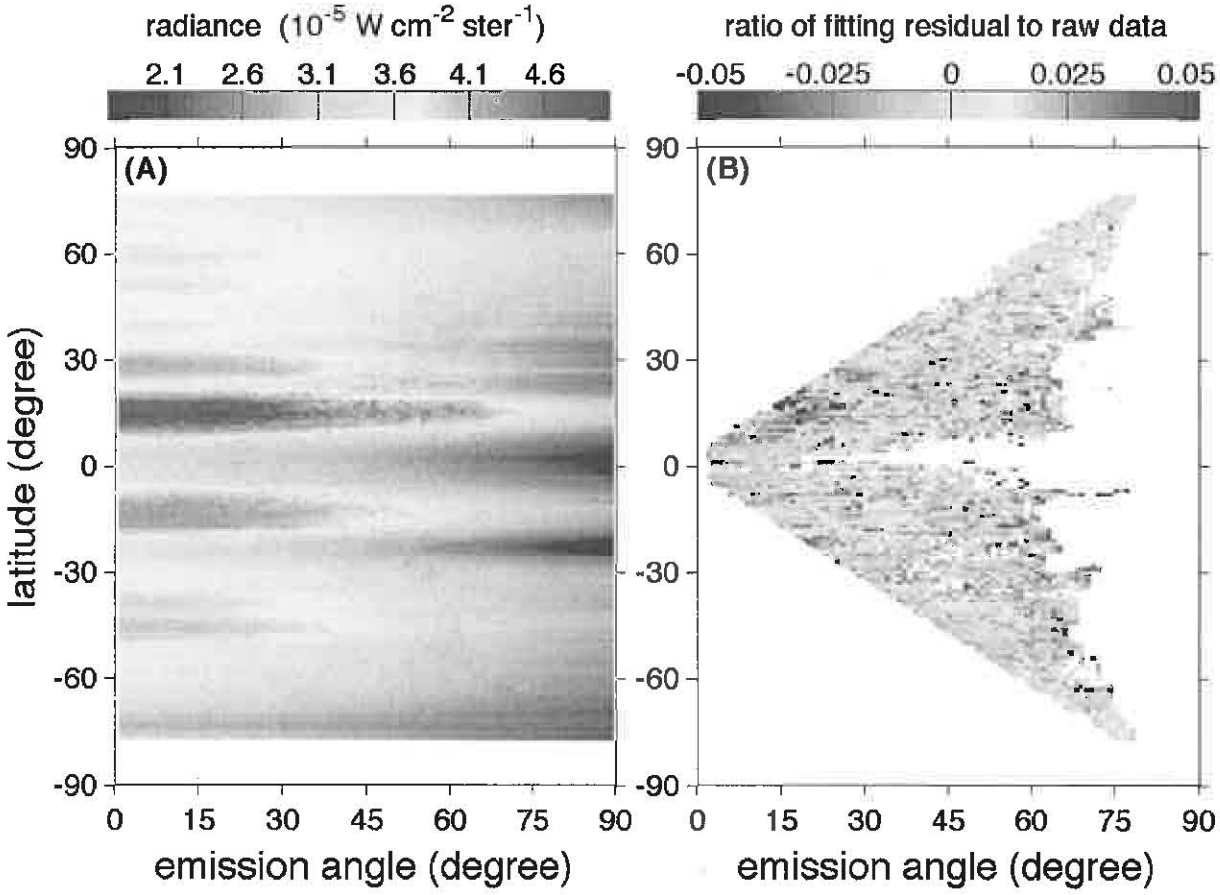
radiance (10^{-5} W cm^{-2} ster^{-1})
2.1 2.6 3.1 3.6 4.1 4.6
ratio of fitting residual to raw data
-0.05 -0.025 0 0.025 0.05
(A)
(B)
latitude (degree)
90 60 30 0 -30 -60 -90
0 15 30 45 60 75 90
emission angle (degree)
emission angle (degree)

Figure 6

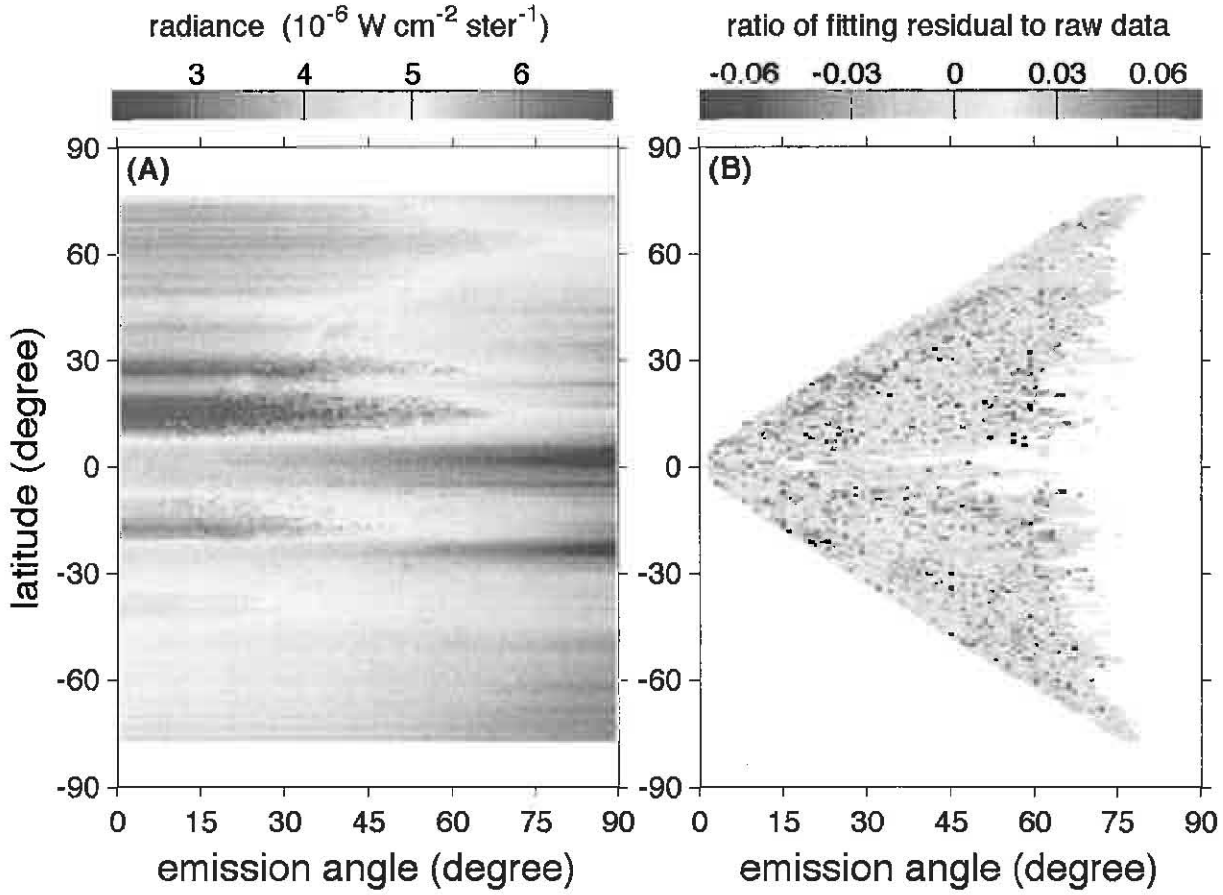
radiance (10^-6 W cm^-2 ster^-1)
3
4
5
6
ratio of fitting residual to raw data
-0.06
-0.03
0
0.03
0.06
(A)
(B)
latitude (degree)
90
60
30
0
-30
-60
-90
0
15
30
45
60
75
90
emission angle (degree)
emission angle (degree)

Figure 7

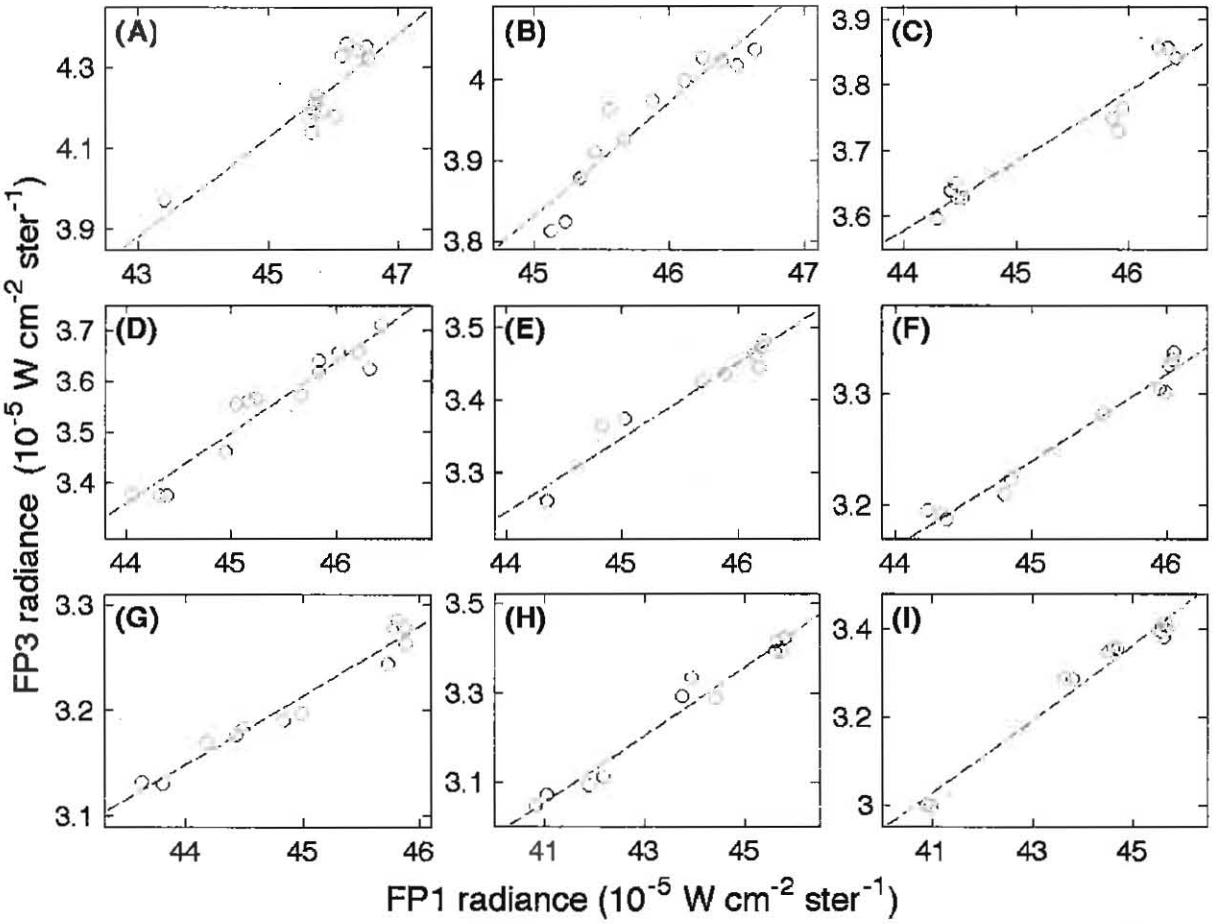
(A)
(B)
(C)
(D)
(E)
(F)
(G)
(H)
(I)
FP3 radiance (10^{-5} W cm^{-2} ster^{-1})
FP1 radiance (10^{-5} W cm^{-2} ster^{-1})

Figure 8

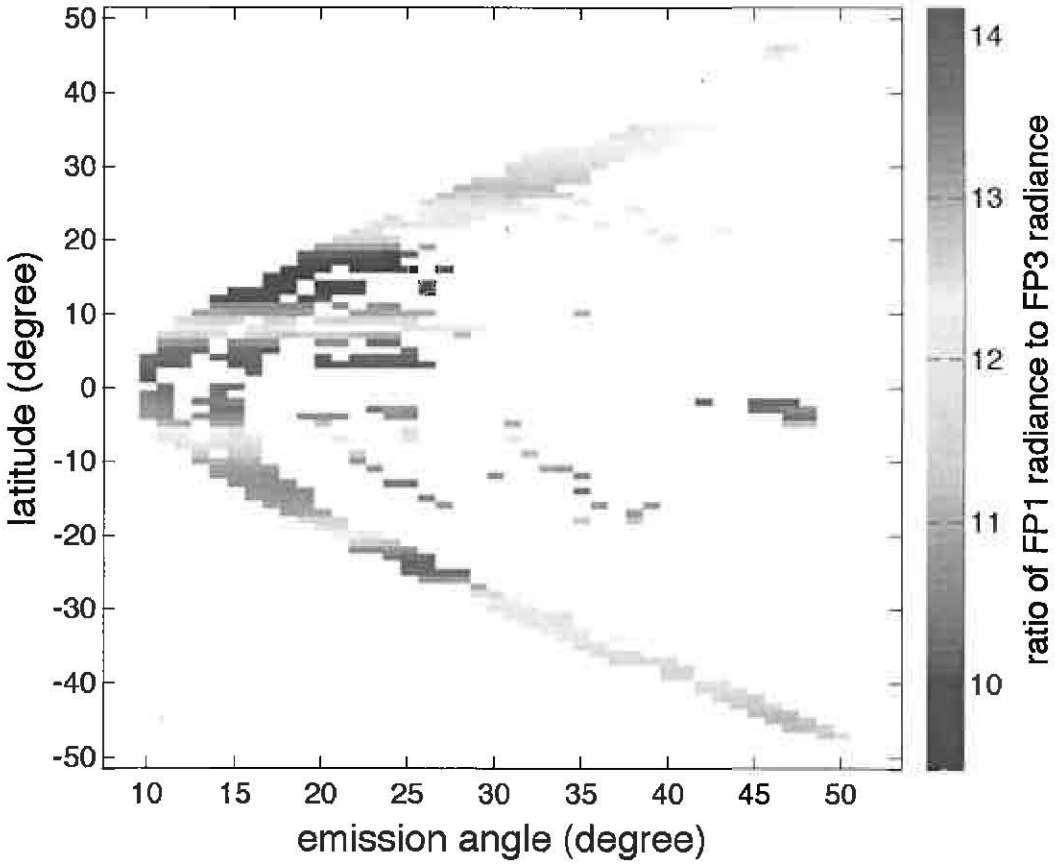
latitude (degree)
50
40
30
20
10
0
-10
-20
-30
-40
-50
10
15
20
25
30
35
40
45
50
emission angle (degree)
14
13
12
11
10
ratio of FP1 radiance to FP3 radiance

Figure 9

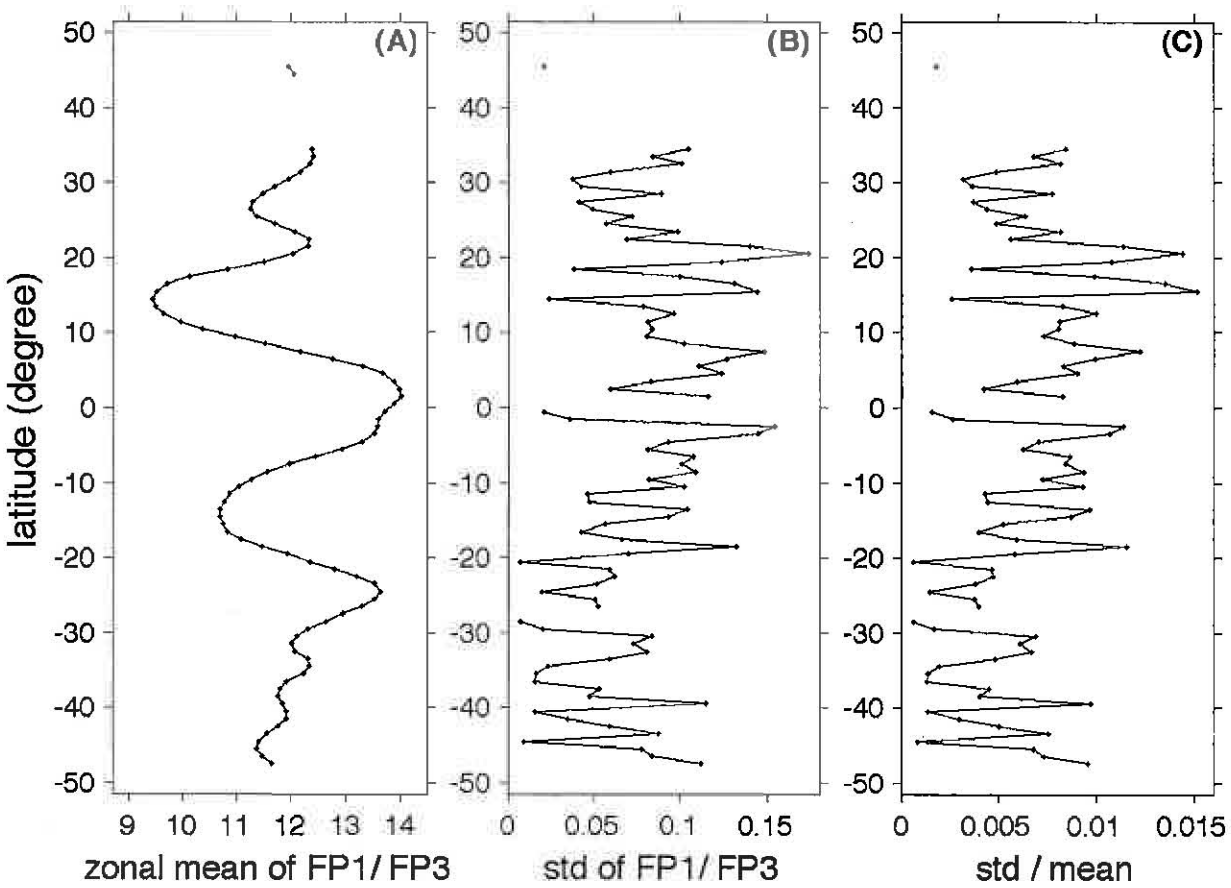
(A)
(B)
(C)
latitude (degree)
50
40
30
20
10
0
-10
-20
-30
-40
-50
9 10 11 12 13 14
zonal mean of FP1/ FP3
0 0.05 0.1 0.15
std of FP1/ FP3
0 0.005 0.01 0.015
std / mean

Figure 10

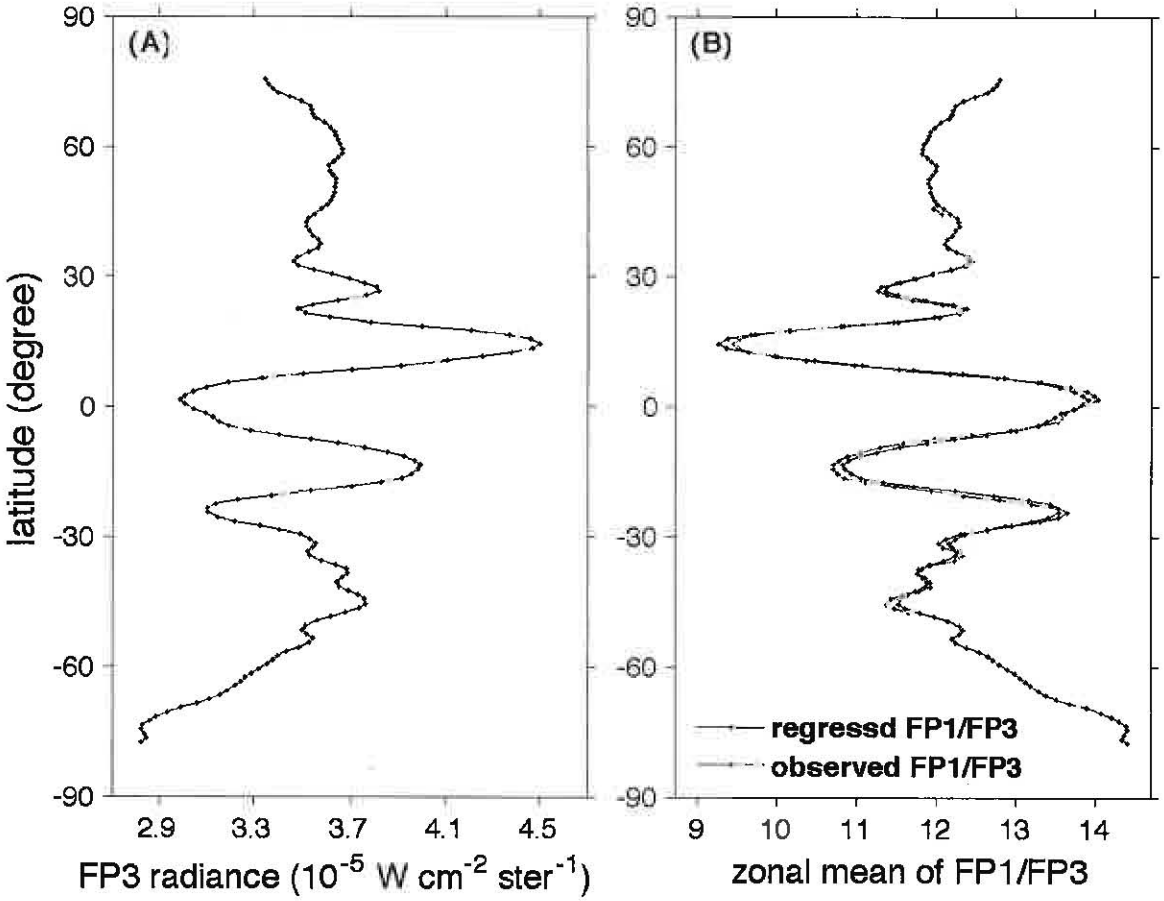
(A)
(B)
90
60
30
0
-30
-60
-90
latitude (degree)
2.9
3.3
3.7
4.1
4.5
FP3 radiance (10^{-5} W cm^{-2} $ster^{-1}$)
9
10
11
12
13
14
zonal mean of FP1/FP3
regressd FP1/FP3
observed FP1/FP3

Figure 11

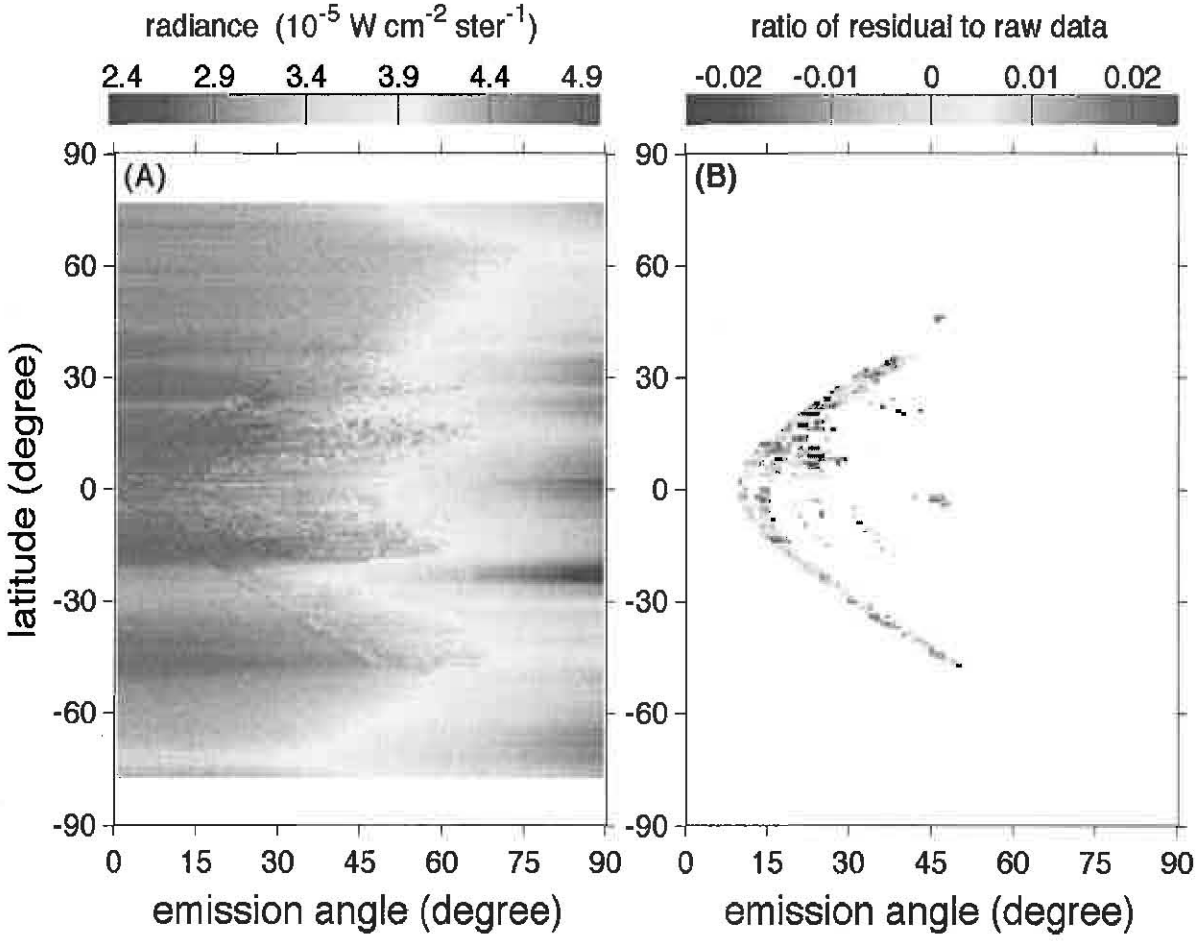
radiance (10^{-5} W cm^{-2} ster^{-1})
2.4 2.9 3.4 3.9 4.4 4.9
ratio of residual to raw data
-0.02 -0.01 0 0.01 0.02
(A)
(B)
latitude (degree)
90 60 30 0 -30 -60 -90
0 15 30 45 60 75 90
emission angle (degree)
emission angle (degree)

Figure 12

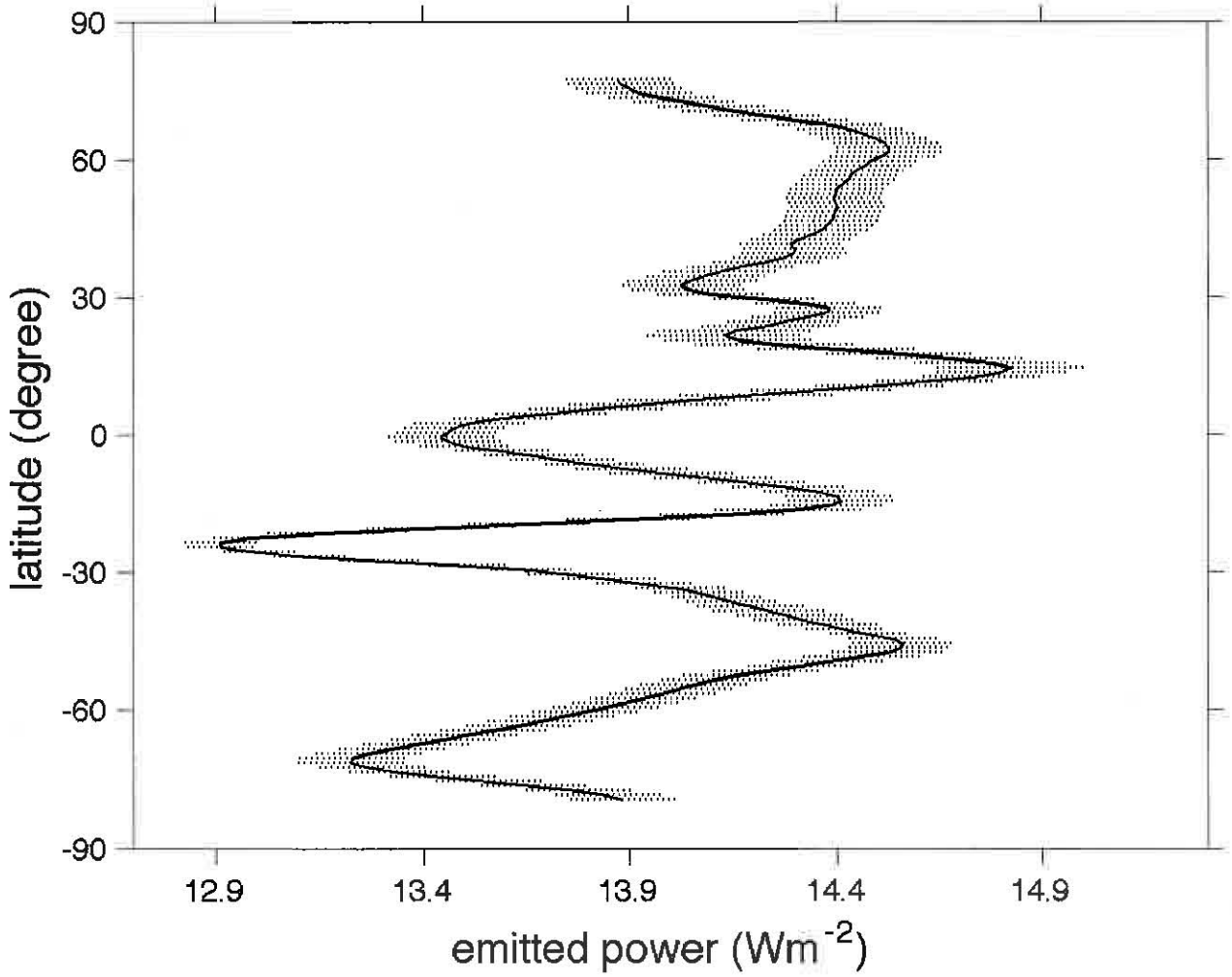
90
60
30
0
-30
-60
-90
latitude (degree)
12.9
13.4
13.9
14.4
14.9
emitted power (Wm-2)

Figure 13

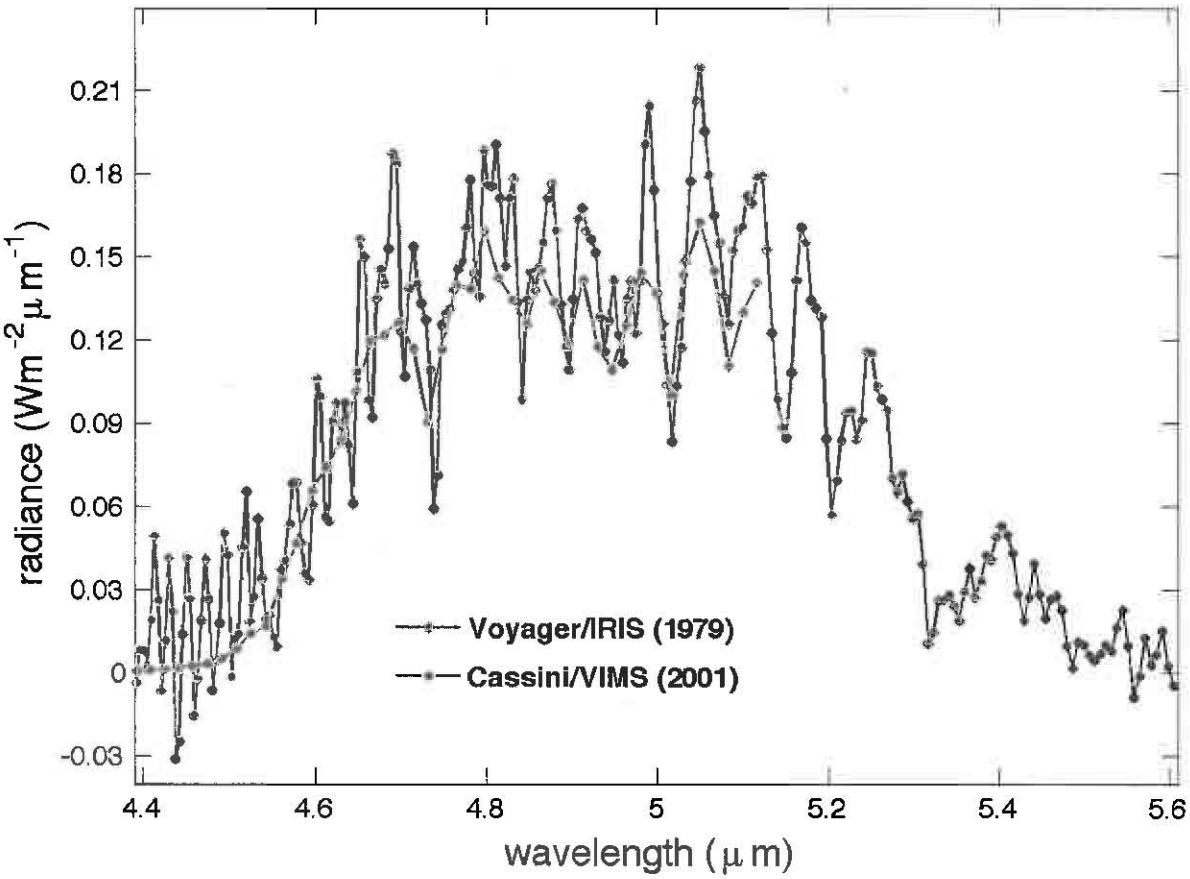
radiance (Wm^{-2}μm^{-1})
0.21
0.18
0.15
0.12
0.09
0.06
0.03
0
-0.03
4.4
4.6
4.8
5
5.2
5.4
5.6
wavelength (μm)
Voyager/IRIS (1979)
Cassini/VIMS (2001)

Figure 14

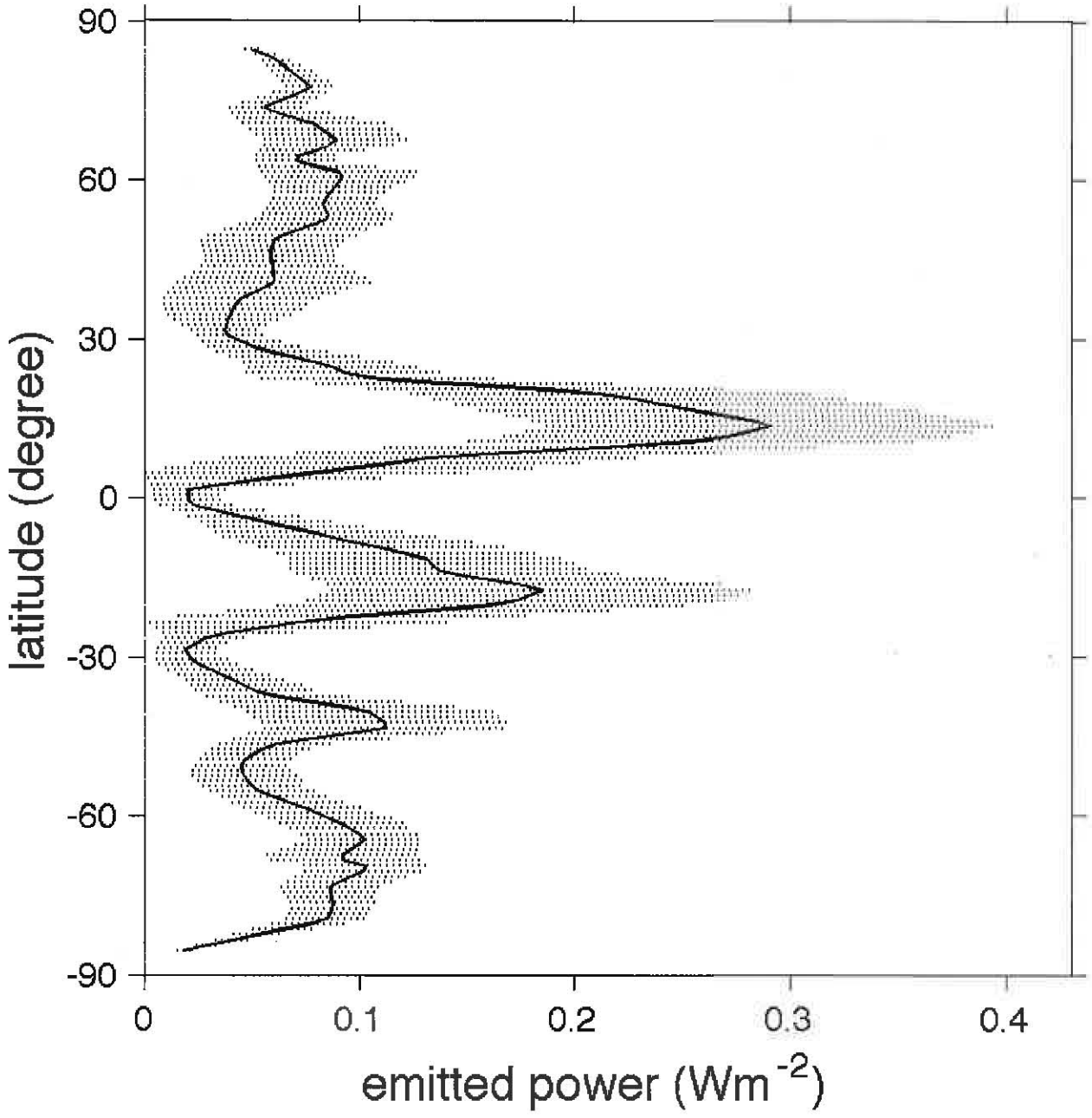
90
60
30
0
-30
-60
-90
latitude (degree)
0
0.1
0.2
0.3
0.4
emitted power (Wm^{-2})

Figure 15

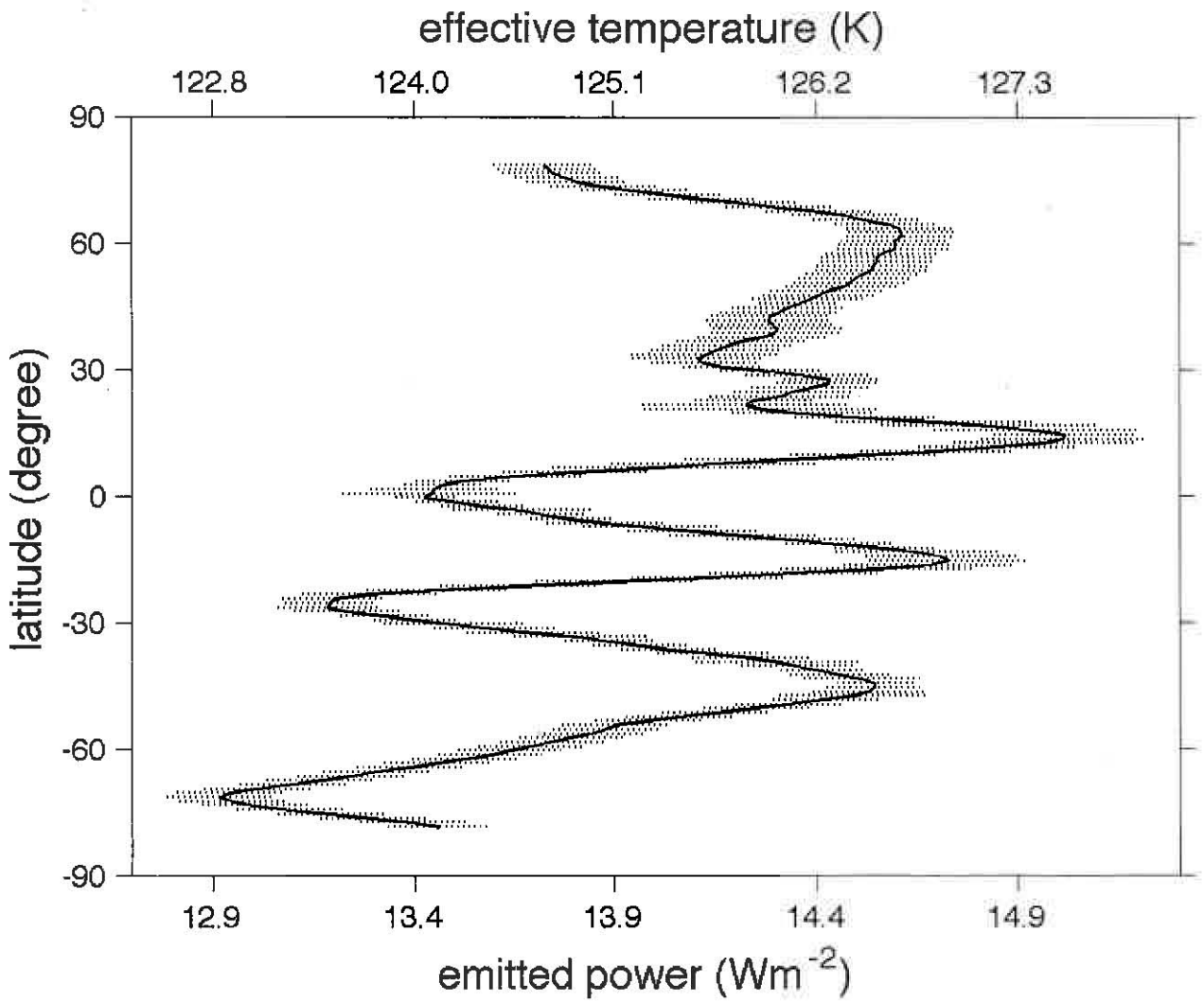
effective temperature (K)
122.8
124.0
125.1
126.2
127.3
90
60
30
0
-30
-60
-90
latitude (degree)
12.9
13.4
13.9
14.4
14.9
emitted power (Wm-2)

Figure 16

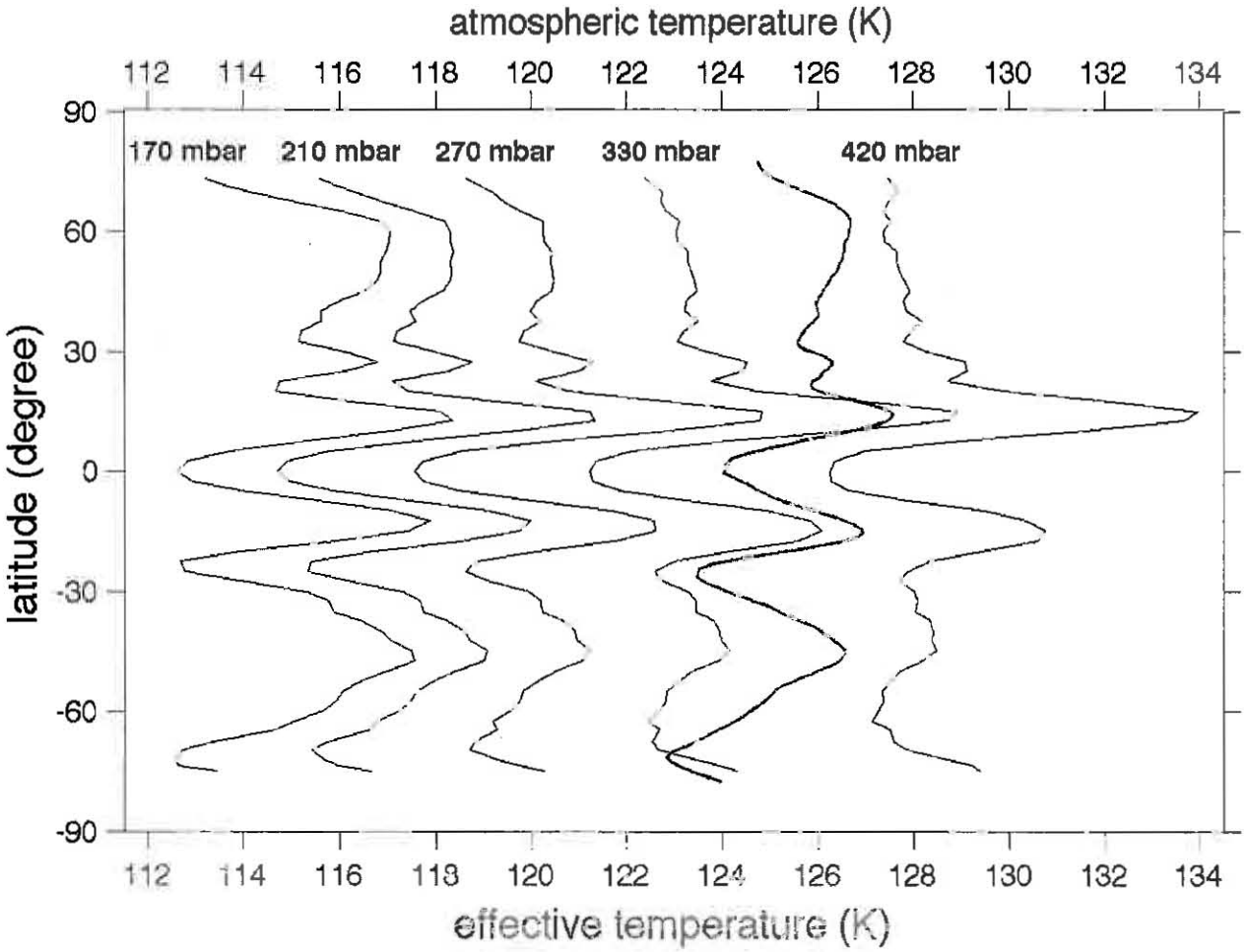

Figure 17

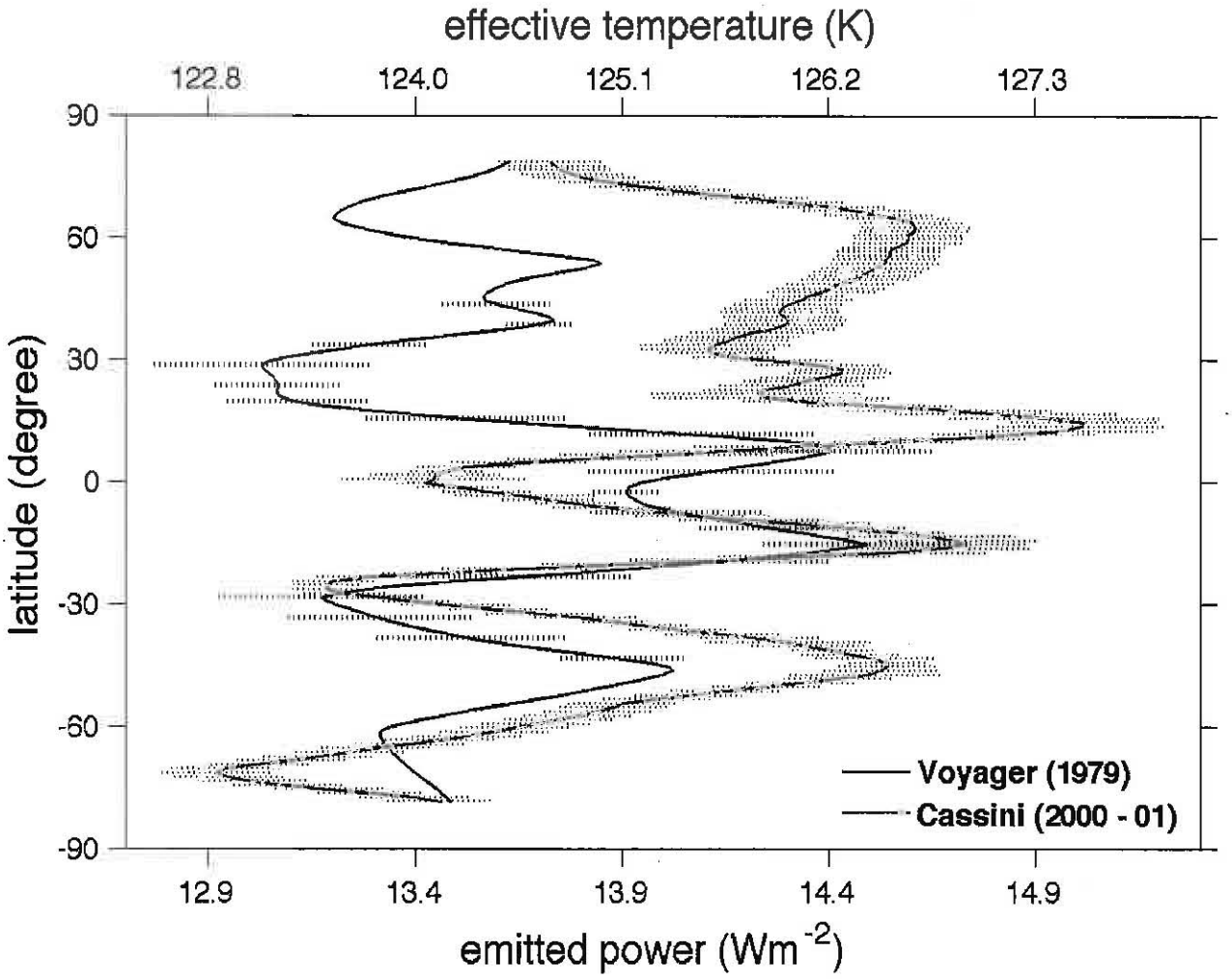
effective temperature (K)
122.8
124.0
125.1
126.2
127.3
90
60
30
0
-30
-60
-90
latitude (degree)
Voyager (1979)
Cassini (2000 - 01)
12.9
13.4
13.9
14.4
14.9
emitted power (Wm-2)

Figure 18

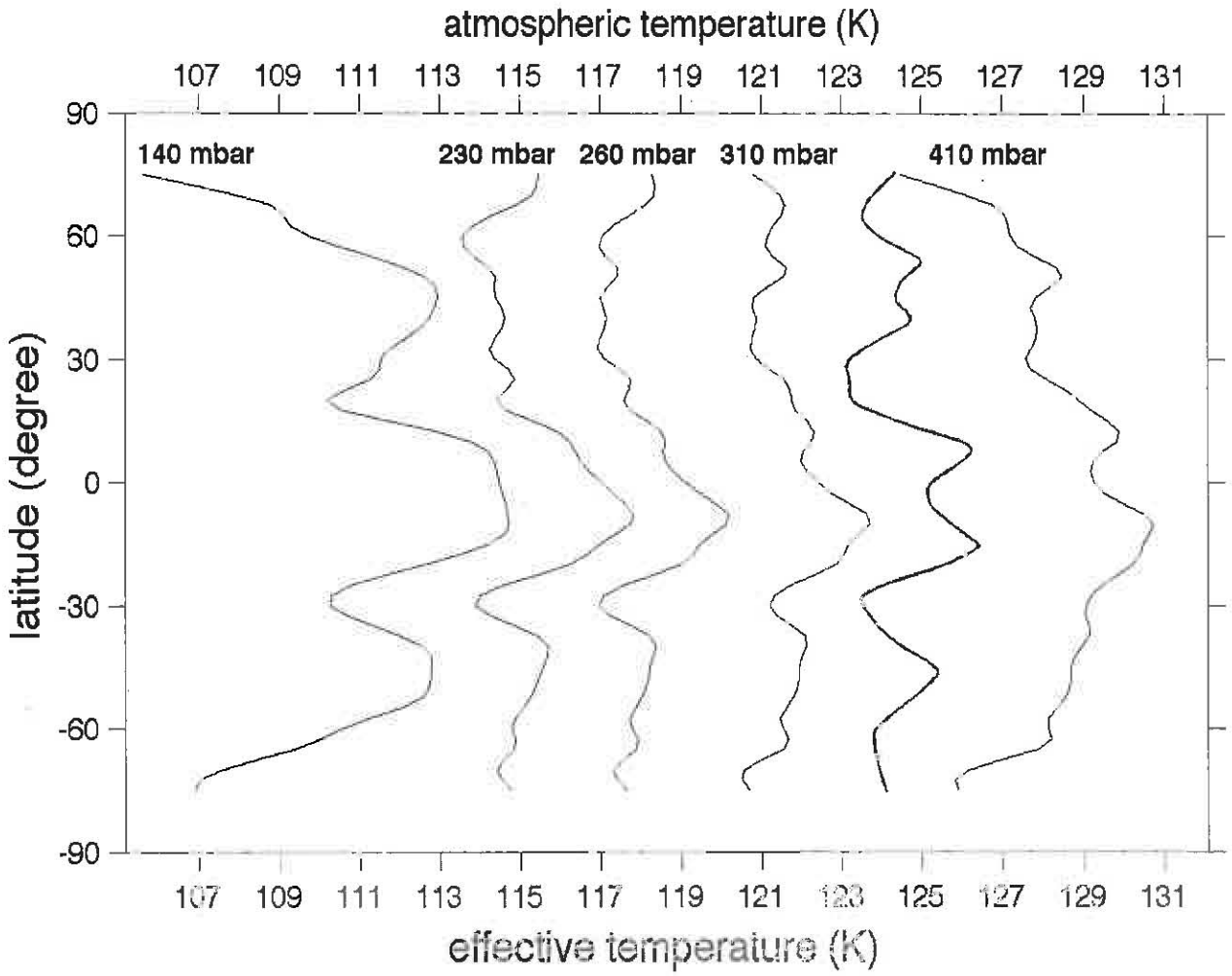
atmospheric temperature (K)
107 109 111 113 115 117 119 121 123 125 127 129 131
90
60
30
0
-30
-60
-90
latitude (degree)
140 mbar
230 mbar
260 mbar
310 mbar
410 mbar
107 109 111 113 115 117 119 121 123 125 127 129 131
effective temperature (K)

Figure 19

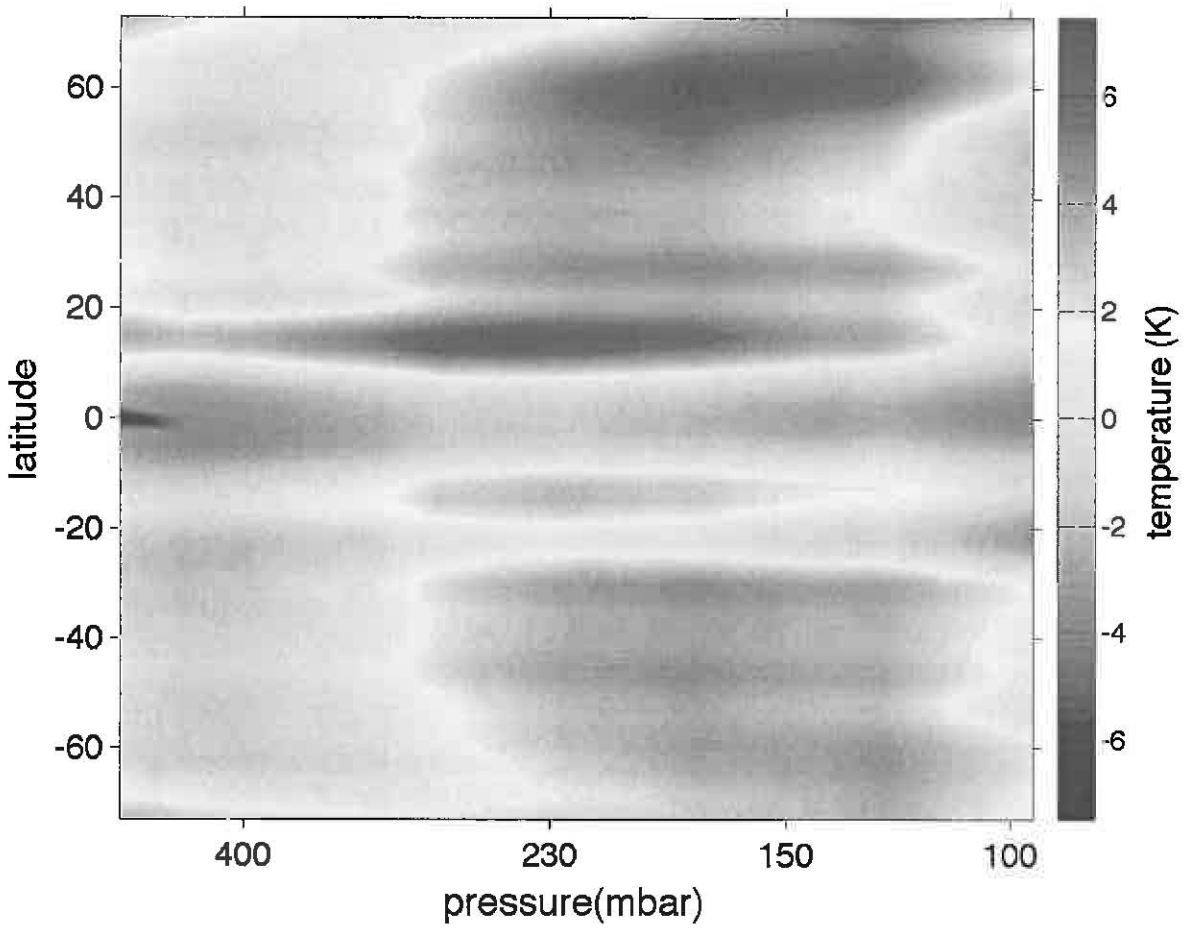
60
40
20
0
-20
-40
-60
latitude
400
230
150
100
pressure(mbar)
6
4
2
0
-2
-4
-6
temperature (K)

Figure 20

1358

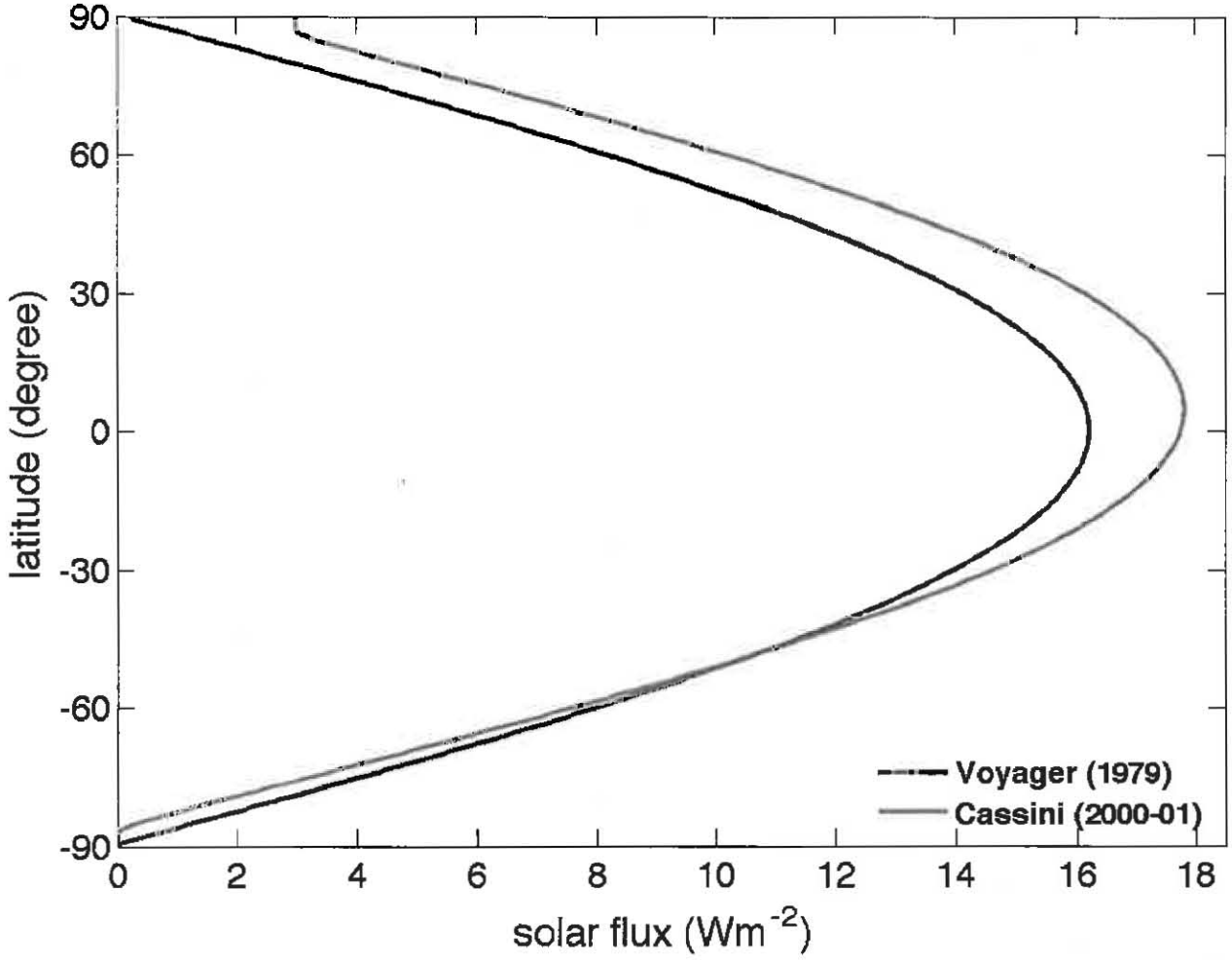

1359
1360